Reactions between simple models of biomolecular compounds and small water clusters of the superoxide anion

Marius Friberg Otterstad

Master's thesis

Faculty of mathematics and natural sciences

UNIVERSITY OF OSLO

15.05.2017

Reactions between simple models of biomolecular compounds and small water clusters of the superoxide anion

2017

Reactions between simple models of biomolecular compounds and small water clusters of the superoxide anion

Marius Friberg Otterstad

http://www.duo.uio.no/

Print: Reprosentralen, Universitetet of Oslo

Abstract

Superoxide anion radical water clusters ($O_2^{\bullet-}(H_2O)_n$) were formed in an ESI and analysed using a QTOF-MS instrument. The quadrupole was used to mass-select the cluster size before entering a collision cell containing the vapour of a model chemical allowing a reaction to occur between the two species. The model chemicals used were dimethyl disulphide (DMDS) and acetic acid. The products were then analysed in a TOF detector. Energy diagrams for the reactions observed were constructed using computational methods. Dimethyl disulphide showed a very low reactivity towards superoxide water clusters other than the formation of adducts. This is likely due to a large energy barrier for the cleavage of the S-S bond in an S_N2 reaction. The determination of the exact geometry and height of this transition state was unsuccessful. When naked superoxide (n = 0) reacted with acetic acid, acetic acid was easily deprotonated, this reaction became less favourable as cluster size increased. As cluster size increased, adduct formation increased which is always accompanied by the loss of at least one water molecule. A hypothesis is proposed that states the endothermic evaporation of a water molecule from the adduct allows for the removal of excess internal energy which stabilizes the adduct which is formed from an exothermic process in an adiabatic environment. Extrapolation of these results indicate adduct formation seems to be very favourable in bulk solution.

Acknowledgments

Although this thesis is result of my many long hours spent behind a computer screen, several others have contributed to it in their own way and deserve credit. I would like to thank Glenn B. S. Miller, for literally being right next to me, teaching me practical things and answering countless questions whenever I had any. Because lab work and experiments are rarely without technical issues, Mauritz Ryding and Osamu Sekiguchi have been of great help when showing me the ropes in the lab and providing tech support whenever an unexpected problem occurred in the lab. As the deadline approached, Joakim Samuel Jestilä was very helpful in providing input on any questions I had about the details of the thesis. A special thanks must be given to my supervisor, Einar Uggerud, for always being a great source of positivity, inspiration and always pointing me in the right direction whenever I was lost. I don't think I could have asked for a better supervisor.

While they may or may not be aware of it, I'd like to extend a big thanks to my family and friends, for helping me relax whenever the stress level was at its highest. Especially my grandparents, Ruth and Rolf, have been very supportive, with their regular and long phone calls, asking questions and trying to understand what I say, despite having limited scientific background.

Thank you all so much.

Table of Contents

1. Introduction

The superoxide anion radical ($O_2^{\bullet -}$), hydrogen peroxide (H_2O_2) and the hydroxyl radical ($OH^{\bullet}$) are the species known as reactive oxygen species (ROS). A radical is a molecule with unpaired electrons, in this case both the superoxide anion radical and the hydroxyl radical has a single unpaired electron. This electron increases the reactivity of the species significantly, but radicals are usually less stable than their non-radical form and can easily deteriorate. Despite their short lifetime, radicals are of great importance to certain reactions and are the cause of oxidative stress. [1]

While these species may be damaging, they are also used as important signaling molecules. [2] ROS can be removed through metabolic processes involving superoxide dismutase, catalase and non-enzymatic antioxidants. [1] This results in a delicate balance between the production of free radicals and their removal. [3] Should ROS production exceed the cell's capacity to remove these species, the excess ROS may start causing one or more uncontrolled reactions which damage structures in the cell, resulting in oxidative stress. While it is not the only factor, it is widely accepted that the accumulation of oxidative stress is contributing to the aging process. [1] Oxidative stress is also considered to contribute to a variety of health issues like cancer, neurodegenerative (such as Parkinson's disease and Alzheimer's disease), dermatological and cardiovascular diseases. [4-6]

1.1 - Production and processing of ROS

Mitochondria (Figure 1) are organelles which are found inside cells and are where the majority of cellular ROS is produced. The electron transport chain in the mitochondria is responsible for about 90% of the cellular production of reactive oxygen species. [1] The electron transport chain plays a very important role in adenosine triphosphate (ATP) regeneration by oxidative phosphorylation of adenosine diphosphate (ADP) and consists of five complexes named Complex I, II, II, IV and V. When active, the electron transport chain transports an electron through each of the complexes, enabling important redox reactions to occur before finally, an ADP molecule is phosphorylated to an ATP molecule. During energy transduction, small amounts of electrons are prematurely "leaked" from primarily complex I and III which allows oxygen to be reduced to the superoxide anion radical which is

considered to be the primary ROS as it can be metabolized into the secondary ROS. The cell regulates the concentration of superoxide anion radicals through the use of the superoxide dismutase (SOD). Superoxide dismutase is a group of enzymes that catalyzes the removal of superoxide anion radicals.

$$2O_2^{\bullet -} + 2H^+ \xrightarrow{SOD} O_2 + H_2O_2 \quad (1)$$

Superoxide dismutase therefore acts as a free radical scavenger which is of great importance to prevent oxidative stress. Experiments performed on mice show reduced amounts of superoxide dismutase leads to increased sensitivity to oxidative stress, while increased amounts usually results in an increased resistance to oxidative stress from high levels of ROS. [7]

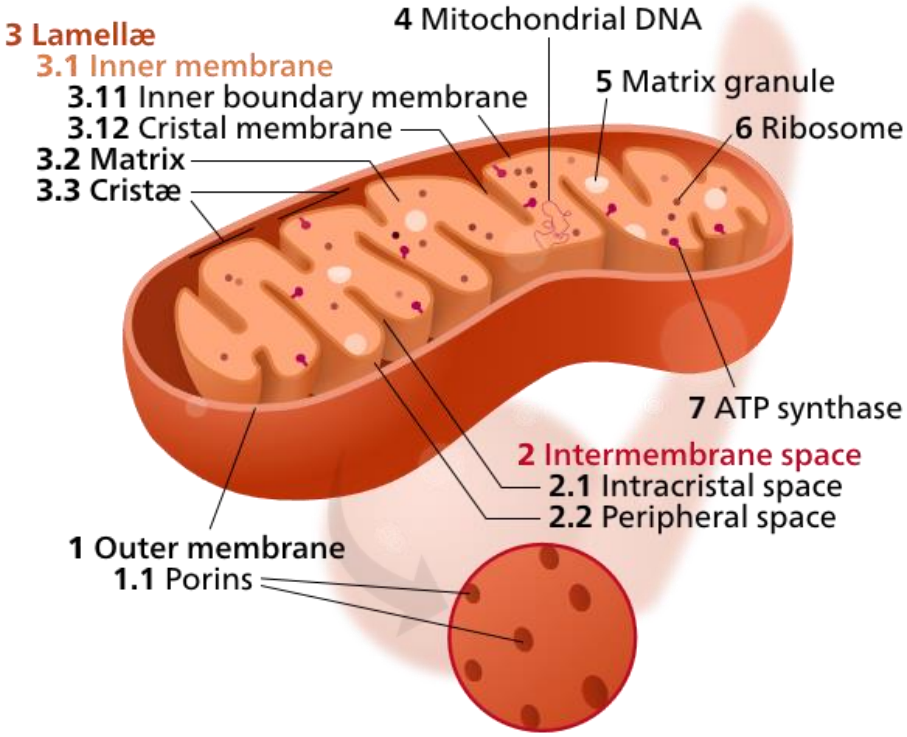

Figure 1: Illustration of mitochondria. The figure shows the general structure of the mitochondria as well as the names of its different components [8].

Three types of superoxide dismutase enzymes are produced in the cell. The first one is superoxide dismutase 1 (SOD1, also known as CuZn superoxide dismutase or CuZnSOD) and is a copper and zinc-containing homodimer which is used for its functionality as an enzyme. The second enzyme is superoxide dismutase 2 (SOD2, also known as manganese superoxide dismutase or MnSOD or FeSOD) which is very similar to SOD1, but uses a manganese or iron cation. SOD1 is for the most part located in the cytoplasm of the mitochondria while

SOD2 is located in the mitochondrial matrix and both SOD1 and SOD2 are present in the intermembrane cytoplasmic space. The most recently characterized superoxide dismutase enzyme is called superoxide dismutase 3 (SOD3, also known as EC 1.151.1) and contains a copper and zinc tetramer and is synthesized with a signaling peptide that directs it to extracellular spaces. [8, 9]

ROS production from the electron transport chain may happen either inside or outside of the inner boundary membrane. Within the inner boundary membrane is the so-called mitochondria matrix (see Figure 1). All ROS leaked from complex I is released into the mitochondria matrix, while complex III releases ROS both inside and outside of the mitochondria matrix. [10] The mitochondrial DNA is located in the mitochondria matrix and therefore, ROS present in the matrix may react with this DNA, damaging it. Mitochondrial DNA (mtDNA) is very vulnerable to damage compared to nuclear DNA (nDNA) as it does not possess the same efficient repair mechanism. [1] Damaged DNA may cause dysfunctional proteins to be created leading to defective subsystems in the mitochondria. This may lead to dysfunctional complex systems in the electron transport chain. Should defective proteins be made for complex I or III, these complexes might proceed to leak even more superoxide into the mitochondria, resulting in an increased superoxide production. This will again lead to increased oxidative stress and creates a vicious cycle of ever increasing ROS production and oxidative stress which will eventually end with programmed cell death. [5]

1.2 - The Fenton reaction

High concentrations of the hydrogen peroxide molecule in the human cells are cytotoxic and processes to safely metabolize hydrogen peroxide are therefore necessary. Hydrogen peroxide does not possess an electric charge, it is not a radical and is generally not very reactive by itself. However, due to its neutral charge can easily pass through a wide selection of biological membranes which charged species such as superoxide may only pass through very slowly. [11] The danger of this specie is its ability to form the hydroxyl radical ($OH^{\bullet}$) which is highly reactive. This may happen though absorption of ultraviolet (UV) light:

$$H_2O_2 \xrightarrow{UV\ light} 2OH^{\bullet} \quad (2)$$

Hydrogen peroxide may also react with a transition metal, for instance Fe^{2+} and a proton to form a hydroxyl radical through the Fenton reaction: [1, 12]

$$H_2O_2 + Fe^{2+} + H^+ \rightarrow H_2O + OH^\bullet + Fe^{3+} \quad (3)$$

Several metal cations may be used in the Fenton reaction (eq (3)), such as cobalt(II) and titanium(III), however, due to the low amount of such metal cations *in vivo*, only Fe^{2+} is the metal cation used for the Fenton reaction *in vivo* under normal conditions. [11] Hydrogen peroxide will react with an unincorporated Fe^{2+} cation or the Fe^{2+} cation in a mononuclear enzyme and undergo the Fenton reaction. The Fe^{2+} cation is then oxidized to Fe^{3+} and hydrogen peroxide is reduced to water and a hydroxyl radical. The superoxide anion radical may also react with iron in mononuclear enzymes with similar results. Fe^{2+} is oxidized to Fe^{3+} in order to reduce superoxide while reacting with two protons to create hydrogen peroxide (shown in equation (4)). If the Fe^{2+} was incorporated in an enzyme, it will dissociate from the enzyme as a result in both reactions.

$$Fe^{2+} + O_2^{\bullet -} + 2H^+ \rightarrow Fe^{3+} + H_2O_2 \quad (4)$$

The loss of this iron cation disables the enzyme which may also be damaged by the hydroxyl radical created by the Fenton reaction. A Fe^{2+} cation can be added to the enzyme to reactivate it again, but the process is not perfect; many repetitions of this activation may cause the enzyme to slowly lose its efficiency due to the damage from the hydroxyl radical. [9]

1.3 - Other sources of ROS

Although ROS produced in a biological system is a big concern, ROS can also be produced from irradiation of species present in the atmosphere. Species present in the in the lower region of the atmosphere (the troposphere) may undergo photochemical reactions and form ROS or secondary organic aerosols (SOA). For instance, hydrogen peroxide may be formed from the photo-oxidation of formaldehyde. This hydrogen peroxide may then be brought down to lower altitudes by rain. [13] Through photolysis of ozone, an oxygen molecule is formed as well as an oxygen atom in its ^1D_g excited state. This excited oxygen can then react with water vapour and produce two hydroxyl radicals. [14]

$$O_3 \xrightarrow{Ultraviolet\ light} O_2 + O^* \quad (5)$$

$$O^* + H_2O \rightarrow 2OH^\bullet \quad (6)$$

These hydroxyl radicals can react with ozone and hydrocarbons to produce ROS and SOA. Gasses such as H_2O_2 are highly soluble species of oxidized species will be removed by the mucus in the upper airways when they are inhaled. SOA (and other ROS associated with such aerosols) on the other hand have different physical properties which allow them to penetrate deep into the lungs and cause oxidative stress. [13]

1.4 – Health issues regarding ROS

Superoxide is mainly generated from the electron transport chain in the mitochondria. The electron transport chain is an important part of the ATP production in the cell and an increased energy demand will result in an increased activity in the electron transport chain. Since superoxide leaks from complex I and III in the electron transport chain, an increase in the production of ATP from this system results in an increase in production of superoxide due to increased activity in the electron transport chain. The brain is metabolically very active and requires a relatively large amount of ATP in order to function properly due to all the neurons located in the brain. The cells in the brain therefore produce more ATP than most organs, resulting in an increased activity in their electron transport chain. This increased ATP production leads to a greater superoxide production in the brain which again leads to increased production of secondary ROS. In addition, iron-containing proteins are found throughout the brain such as cytochromes and ferritin. While most of the iron found in the brain is stored in ferritin, making it less likely to produce hydroxyl radicals compared to free iron cations, brain tissue easily releases iron and copper ions which are capable of producing hydroxyl radicals from hydrogen peroxide, lipid peroxidation and autoxidation of neurotransmitters. The brain's cerebrospinal spinal fluid does contain transferrin which is capable to bind free iron, but calculations indicate transferrin is often close to or is saturated with iron. [15] The brain also has a lower capacity to repair cellular damage and is therefore believed to be more vulnerable to the effects for ROS. This is of interest when studying neurodegenerative diseases such as Parkinson's disease

and Alzheimer's diseases. Patients with these diseases have been reported to have neurodegeneration in selective parts of their brain which is assumed to be a result of oxidative stress. [5] Needless to say, superoxide is greatly tied to the occurrence of such health issue.

1.5 – Superoxide

As mentioned in previous sections, superoxide is of vital importance when discussing oxidative stress. Superoxide is made through monovalent reduction of O_2.

$$O_2 + e^- \leftrightarrow O_2^{\bullet -} \quad (7)$$

A recent review published by Maan et al., 2016 gives a good overview of the properties and production of the superoxide anion and some of their reports will be mentioned here. [16]

Superoxide has been studied in both the condensed phase and the gas phase. [17-20] The lower limit of the lifetime of superoxide is has been estimated by computational methods to be approximately 30ps, which is in good agreement with experimental data. [21] The short half-life of superoxide makes quantitative measurements difficult and maintaining superoxide in a stable state long enough for a measurement to complete can be a difficult task. Several methods are capable of producing superoxide, most notably electrochemical methods such as electrospray ionization which has proven to be a good method for producing superoxide. [18] When an electrospray ionizer is combined with a quadrupole time-of-flight mass spectrometer (QTOF-MS), the ions may be passed through a collision cell where a reaction may occur with a collision gas before superoxide dissociates, making it an excellent method to investigate superoxide reactions in the gas phase.

Superoxide has many interesting properties, such as being a good nucleophile for S_N2 reactions, a good proton acceptor and electron donor, making superoxide a very interesting specie for scientists to investigate. [16] For instance, superoxide has been used to cleave a disulphide bond with the help of an iron cation. [22] This raises the question if superoxide can cleave disulphide bonds in a biological system and if so, what other bonds can it cleave? Answering these questions will provide valuable insight into

superoxide's behaviour *in situ* and its role in processes the cause oxidative stress.

1.6 – Cluster chemistry

It is well-known that species in the atmosphere and ambient air can be ionized by cosmic radiation and radioactive sources such as radon. [23] Oxygen, with an electron affinity of 0.45 eV, can easily be ionized by such radiation to form the superoxide anion radical which can be hydrated by nearby water molecules, forming $O_2^{\bullet-}(H_2O)_n$ clusters. The reactivity of this specie towards CH_3X (X = Cl, Br) has been investigated by Mauritz Ryding and in his paper he concluded that while superoxide can undergo and S_N2 reaction with these species, the energy barrier for this reaction is increased with solvation. [18] This gives a clear indication that hydration of species may affect their reactivates, which is in agreement with previous studies. [24]

As discussed previously, the reactivity of superoxide is of great importance when mapping oxidative stress *in situ*. When superoxide is produced *in situ*, it is hydrated by the water present. Investigating processes in bulk is very expensive when using computational methods due to the large number of solvent molecules that need to be computed. Instead, investigating the system in gas phase and gradually adding more water molecules to the system and then extrapolating those results to bulk phase can give some indication of how the system will perform when in the bulk phase. This allows for characterization of trends that occurs as hydration increases and is a technique that has employed when for instance investigating the solvation effect on metal ions. [25] In a similar fashion, superoxide can be hydrated through the use of an electrospray combined with a quadrupole to filter out a selected cluster size, allowing for careful selection of a specific cluster size. By then passing these clusters through a collision cell containing a gas with a certain type of bond or functional group, the cluster can react with the gas.

In addition, hydration of ions has been proven to have stabilizing effect on the ions. [26] This is especially useful for unstable ions with a short lifetime, such as superoxide, as it allows the production of the ions to become more favourable.

1.7 – The aim of this study

1.7.1 – Dimethyl disulphide

As mentioned in section 1.5, superoxide has been found to be able to cleave a disulphide bond, but the question still remains if this is possible in a biological environment. Due to the high water affinity of superoxide it is likely to be hydrated if water is present, which may alter its reactivity towards the disulphide bond. A hypothesis this study will test is whether or not superoxide at various hydration is able to cleave the disulphide bond in dimethyl disulphide in the gas phase.

1.7.2 – Acetic acid

In a protein, hydrogen bonds between the carboxylic acid groups on the side chains of amino acids are formed to give the protein its secondary structure. Should the carboxylic acid group be deprotonated, the group will no longer be able to act as a hydrogen donor to the hydrogen bond. Should both groups in the hydrogen bond be deprotonated, they will no longer be able to form a hydrogen bond with each other. A suitable model molecule for a carboxylic acid is the acetic acid molecule. In the gas phase, superoxide has a higher proton affinity than acetate, thus superoxide is able to deprotonate acetic acid, but the effect hydration has on this reaction has not been studied. [27] The second hypothesis to be tested in this study is if hydration of the superoxide anion radical will hinder this deprotonation reaction in the gas phase.

2. Instrument setup

All experiments were conducted on a Waters Quadruple Time of Flight 2 W Mass Spectrometer (QTOF-MS). The various components of this instrument and how they were used will be explained now.

2.1 - Electrospray Ionization

Electrospray ionization (ESI) is a so-called “soft” ionization method. “Soft” ionization methods primarily ionize the compounds without destroying their structure. This method also allows for the transformation of a solution into an aerosol, which is required in order to analyse the compounds in a mass spectrometer. When combined with a mass spectrometer, this allows us to much more easily produce and detect the molecular ion, giving us the mass of this molecule. Its counterpart, “hard” ionization methods, tends to destroy and fragment the compound during the ionization process. This allows us to observe the fragments of the molecular ion, which have a range of uses. However the signal of the molecular ion is typically very weak when using these methods. The fragmentation pattern of a compound can be used to determine the structure by comparing the pattern to a library of fragmentation patterns of known compounds (such as the NIST library). [28]

In the first step, the solution containing the analytes is passed through a capillary which is in a region of atmospheric pressure while a high voltage (U_{cap}) is applied between the capillary and the entrance to the mass spectrometer. Due to this potential, when the liquid exits the capillary it forms what is known as a Taylor cone. At the tip of the cone, charged droplets are formed, released and pulled towards the opening to the mass spectrometer (Figure 2). The ESI can form both positive and negative ions by simply switching the polarities of the voltage applied to the capillary and the opening to the mass spectrometer. U_{cap} was chosen to be 3.30kV, but could be reduced to 2.90kV if the signal of the ion of interest was too strong. One droplet may have a charge which is greater than one. A nebulizer gas (also called drying gas and is shown as N_2 in Figure 2) is ejected from the sides of the capillary and is often an inert gas such as nitrogen or argon gas. This gas helps the solvent evaporate, thus reducing

the size of the droplets. Desolvation gas (N_2 was used for the experiments in this paper) can also be turned on to further increase the evaporation of the solvent. As the size of the droplets get smaller, the distance between the charges is reduced and the repulsive force between the charges increases. Two forces are acting in the droplet; the surface tension trying to hold the droplet together, and the coulombic forces from the charges inside the droplet trying to burst the droplet. When these two forces become equal each other, the breaking point which is known as the Rayleigh instability limit has been reached. Should the droplet size be reduced further and pass the Rayleigh instability limit, the coulombic forces will overcome the surface tension and the droplet will burst in a coulombic explosion, forming smaller droplets with a lower charge. [29]

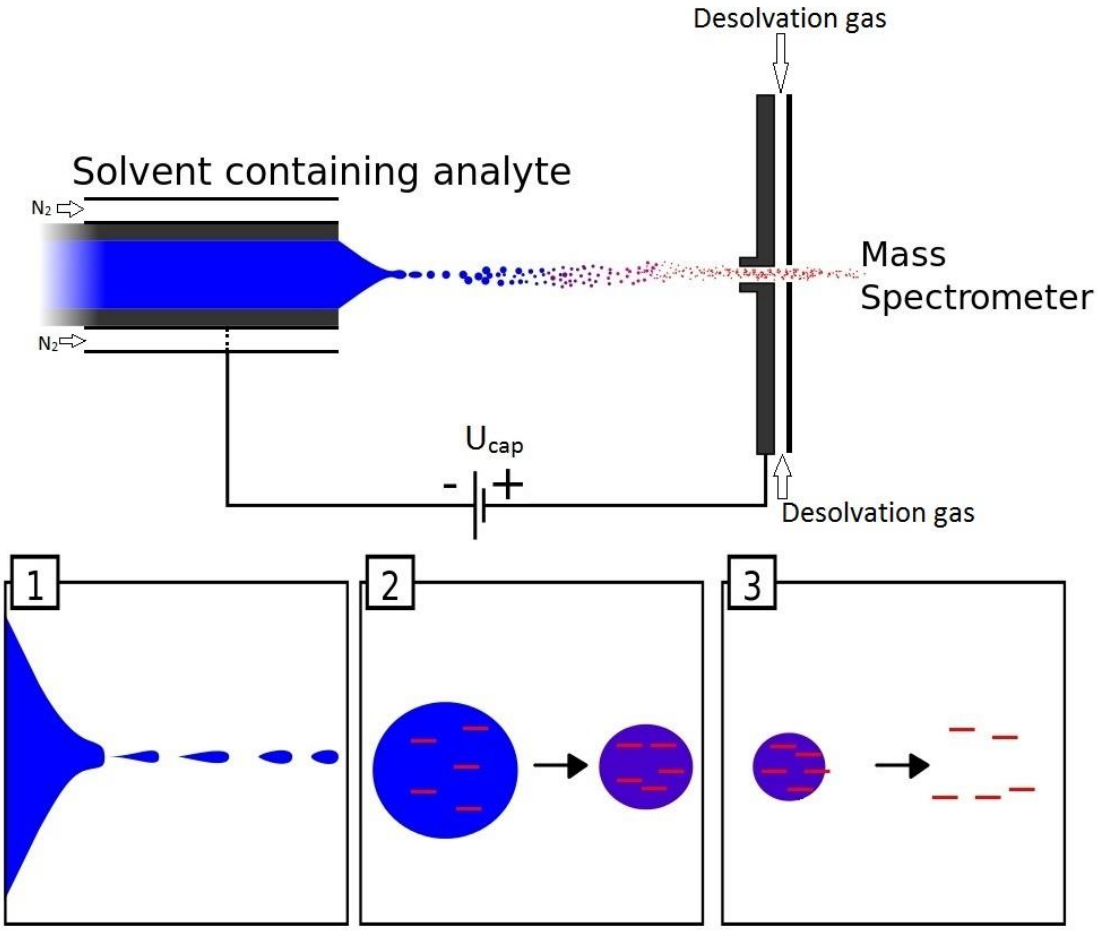

Figure 2: Diagram of Electrospray Ionization. [30]

The maximum number of charges (Z_{R^e}) that can be stored inside a droplet while still keeping the droplet stable is given by the Rayleigh equation:

$$Z_{R^e} = \sqrt{8\pi(\epsilon_0 \gamma R^3)} \quad (8)$$

Where R is the spherical radius of the droplet, γ is the surface tension and ϵ is the permittivity of the surrounding solvent. [31]

The smaller droplets that are formed then undergo the same process of solvent evaporation and coulombic explosion. This process continues until only the analyte and the charge remains, which then enters the mass spectrometer. Small amounts of the solvent may still be present on the charged analyte, this will however change the mass of the ion and can be filtered out through a mass selection unit in the mass spectrometer.

Through this process, superoxide anions and water clusters of this anion is able to be produced and fed to the mass spectrometer. The nitrogen gas used contained some oxygen, which actually improved the superoxide production compared to when pure nitrogen gas was used.

2.2 - Quadrupole mass analyser

The quadrupole consists of four linear, parallel, metal rods with equal distance apart, having a distance r_0 from the center and a constant stream of ions passes in the middle between all four rods. While active, two rods on opposite sides have the same DC current passing through them (U), while the remaining two rods have the DC current passing through it, but with opposite sign (-U). Both rod pairs also have an AC component (V), adding to their potential. The AC component is periodic, with a radio frequency (RF) denoted as ω. The total potential is given by

$$\phi_0 = U + V \cos \omega t \quad (9)$$

The ions enter the quadrupole with a velocity that's parallel to the z-axis and once inside the electric field, the ion will accelerate along the x- and y-axis. Because the potential changes over time, the attraction and repulsion in the x-

and y-axis will alternate. The motion of the ion in along the x- and y-axis is described by equations (10) and (11).

$$\frac{d^2x}{dt^2} + \frac{e}{m_i r_0^2}(U + V\cos\omega t)x = 0 \tag{10}$$

$$\frac{d^2y}{dt^2} + \frac{e}{m_i r_0^2}(U + V\cos\omega t)y = 0 \tag{11}$$

While the ions may not have a stable trajectory through the quadrupole, as long as its amplitude in the xy-plane is not too large, the ions will not get discharged by hitting the poles and instead just pass through. The conditions for this can be found using the Mathieu equations. When written in dimensionless terms, equation (10) and (11) yields the following equations:

$$\frac{d^2x}{d\tau^2} + (a_x + 2q_x\cos 2\tau)x = 0 \tag{12}$$

$$\frac{d^2y}{d\tau^2} + \big(a_y + 2q_y\cos 2\tau\big)y = 0 \tag{13}$$

When comparing equations (12) and (13) to equations (10) and (11), expressions for the parameters a and q can be obtained.

$$a_x = -a_y = \frac{4eU}{m_i r_0^2 \omega^2} \tag{14}$$

$$q_x = -q_y = \frac{2eV}{m_i r_0^2 \omega^2} \tag{15}$$

$$\tau = \frac{\omega t}{2} \tag{16}$$

By adjusting ω, U and V, a certain m/z value or m/z range will have a stable trajectory through the quadrupole (i.e. the amplitude of the oscillations of the ions is less than r_0). By making a plot of a vs q, a stability diagram is obtained, showing when the trajectories along both the x- and y-axis are stable, when the trajectory along either the x- or y-axis is stable, or when neither trajectories are stable (see Figure 3). By adjusting the U and V voltage, while still keeping their ratio constant, a very narrow interval of m/z values may have a stable trajectory through the quadrupole, so narrow in fact, that only a certain m/z value can pass through. [29, 32]

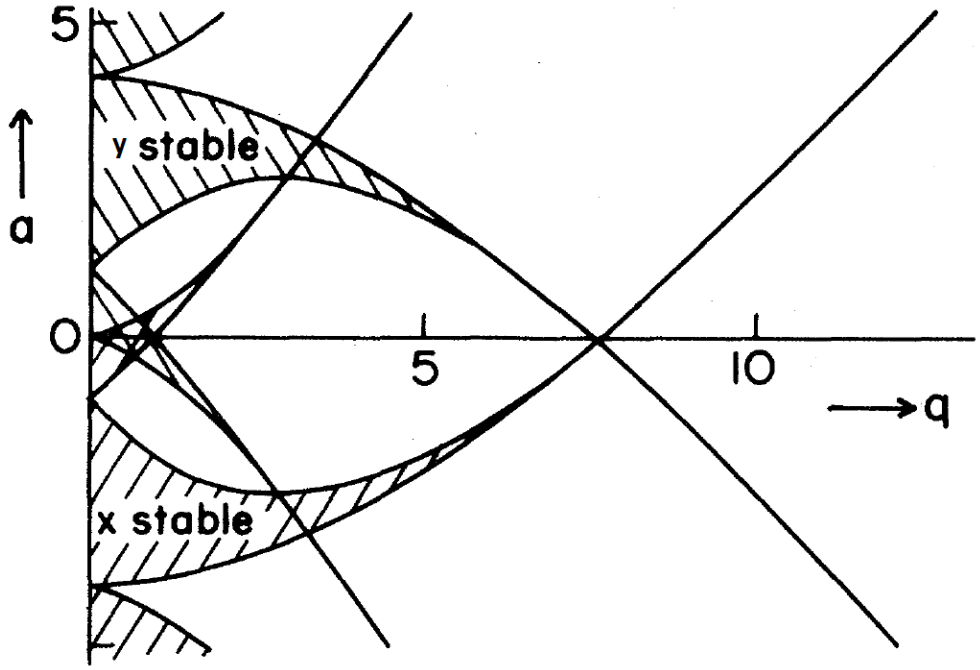

Figure 3: Stability diagram in the xy-plane of a quadrupole field. Reprinted figure with permission from reference [33] Paul Wolfgang, Reviews of Modern Physics, Volume 62, page 531-540, 1990. Copyright 1990 by the American Physical Society.

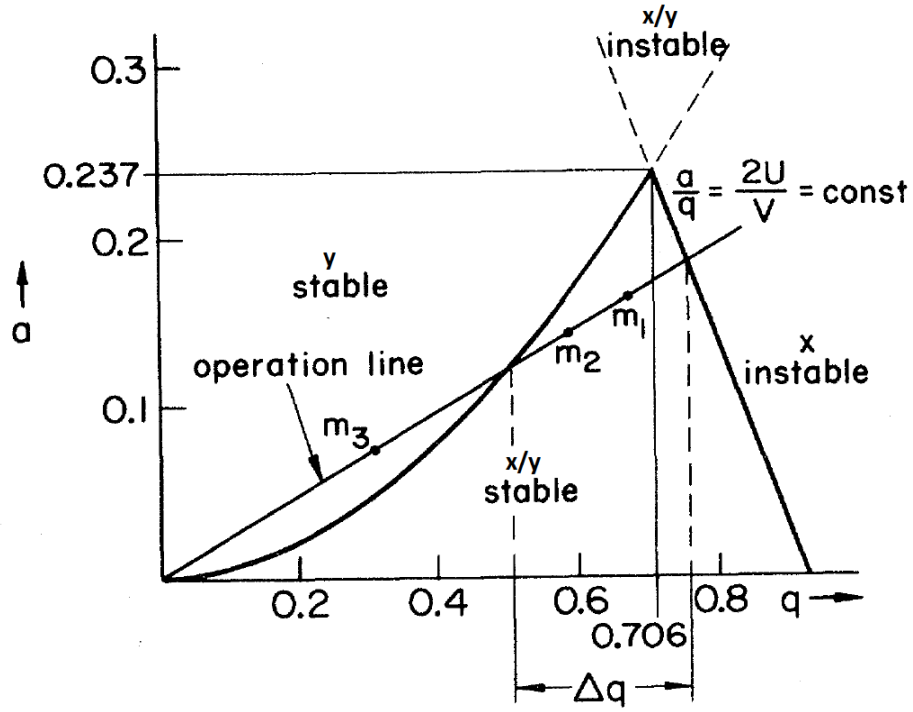

Figure 4: Stability diagram which ions are stable in both the x and y directions. Only masses inside the triangle have a stable trajectory through the quadrupole. Reprinted figure with permission from reference [33] Paul Wolfgang, Reviews of Modern Physics, Volume 62, page 531-540, 1990. Copyright 1990 by the American Physical Society.

By using the quadrupole to only accept a certain m/z value, only clusters with a specific n-value was able to pass through and guided into the collision cell, where it could react with the reagent present. In the case of these experiments, the quadrupole was used to only allow desired cluster sizes of n = 0 - 4 to pass through the quadrupole, which has masses of 32, 50, 68, 86 and 104 respectively. By adjusting the quadrupole to only accept one of these masses, only that specific cluster could then enter the collision cell. The water clusters that are accepted by the quadrupole and enter the collision cell will be referred to as the molecular ion for simplicity.

2.3 - Collision cell (hexapole)

Multipoles can also be used to guide ions through the instrument by making small adjustments to the quadrupole. The quadrupole has two potentials, the DC and RF potentials. Should the DC voltage U be set to zero, only the RF voltage would make a contribution to the potential. This causes the quadrupole to allow a wide range of ions to pass through (see Figure 4: Stability diagram which ions are stable in both the x and y directions. Only masses inside the

triangle have a stable trajectory through the quadrupole. , if the DC potential is turned off, i.e. a = 0, a wide range of m/z values will be allowed through the multipole). This can also be used on hexapoles (6 poles instead of 4) and octapoles (8 poles instead of 4); however these devices cannot be used be used to selectively allow a narrow interval of m/z values to pass through. This is due to the fact that hexapoles and octapoles do not have a sharp cut-off transmission for various m/z values.

These higher-order RF-only 2N-multipoles have a steeper potential well, which gives them an increased interval of accepted m/z values and better ion guiding capabilities (deeper potential well) than what a quadrupole can offer. Therefore, these higher-order RF 2N-multipoles are used as ion-guiders trough the instrument. Because neutral ions are not affected by the multipoles, and can freely exit the potential well between the poles and be pumped out of the collision cell, while ions are kept trapped within the potential well within the multipole.

By using a higher-order RF-only 2N multipole to guide the ions into and through a chamber containing a collision gas, the ions may react or fragment as a result of collisions with the collision gas. The product-ions produced from this process are kept within the multipole and guided to a mass analyser and detector for analysis. In this case, a time of flight detector was used to analyse the mass of the ions.

A barometer is placed inside the collision cell to allow for pressure measurements during experiments. The unit of the pressure can be given in the form of different gasses, in the case of these experiments, the H_2O unit was used. Because the pressure in the collision cell needs to be low in order to function properly, gas is continuously pumped out of the cell. This causes the pressure to not be homogenous throughout the cell. In order to increase the efficiency of this setup, the gas inlet and barometer is placed very close to the multipole, ensuring the pressure is the highest where the ions are. This setup however and lack of homogeneousness of the pressure means the observed pressure reported by the barometer can depend on which instrument is used and should be considered when attempting to reproducing the pressure conditions with different instruments. [32, 33]

2.4 - Collision energy

When ions collide with the collision gas in the collision cell, a reaction may occur. What reactions occur may be strongly dependent on the internal energy of the species during the collision. Careful control of the energy of the species can therefore be of great importance when investigating various reaction pathways. This is very important for collision induced dissociation (CID). When considering CID, a species AB^+ is introduced to the collision cell. When AB^+ collides with a neutral gas N, the species becomes activated, forming AB^{*+}. The internal energy of the activated species is then randomly distributed throughout the system, before dissociating into A^+ + B. The reaction equation is shown in equation (17).

$$AB^+ + N \rightarrow AB^{+*} + N \rightarrow A^+ + B + N \quad (17)$$

The internal energy of the system E_{AB+*} is composed of the energy before the collision, E_{AB+}, and any energy transferred during the collision, Q.

$$E_{AB^{+*}} = E_{AB^+} + Q \quad (18)$$

If the molecular ion has no metastable decomposition, all the molecular ions are due to field ionization. This means all the energy of the molecular ion is from the ionization process. By considering a reference system where the molecular ion is at rest, (E_{AB+} = 0) any internal energy available for the fragmentation process will be due to the transferred energy Q during the collision. The maximum energy that can be transferred during the collision forms an upper limit for the energy available for the fragmentation process. This upper limit for Q is called the center-of-mass energy and is defined by equation (19):

$$E_{com} = E_{LAB} \frac{m_N}{m_N m_{AB}} \quad (19)$$

In this equation E_{LAB} is the ion kinetic energy in the laboratory frame of reference, m_N is the mass of the neutral gas molecule and m_{AB+} is the mass of the ion.[35] When using the instrument, the E_{LAB} can be adjusted to get the desired E_{com}.

2.5 - Time of Flight mass analyzer

The time-of-flight mass analyzer (TOF) operates on a simple concept; heavier ions move more slowly than lighter ions, given they have the same kinetic energy. A continuous stream of ions consisting of products and unreacted species exits the collision cell and enters TOF region along the x-axis. An orthogonal accelerator is positioned parallel with the ion stream and pulses with an electromagnetic field (usually 5-10 kV, although due to the low mass of the ions analysed in the experiments, this was set to 3.00kV) of the same polarity of the ions. When the pulse is turned on, the ions in the ion beam currently positioned over the accelerator are accelerated along the y-axis by the field generated by the accelerator for the duration of the pulse. This gives the accelerated ions the same kinetic energy. The accelerated ions will start moving in the y-direction and eventually hits the detector. The m/z value of the ion can be determined through measuring the time the ions require to reach the detector. The formula used is to calculate the m/z ratio is

$$\frac{m_i}{z} = \frac{2eUt^2}{s^2} \quad (20)$$

Where e is the charge of an electron, U is the voltage applied to the accelerator, s is the distance the ions have to travel, and t is the time the ion is detected after being accelerated.

In addition, an electromagnetic field (also referred to as a reflectron) can be placed at the end of the tube, reflecting the ions back towards a detector (Figure 5). [32]

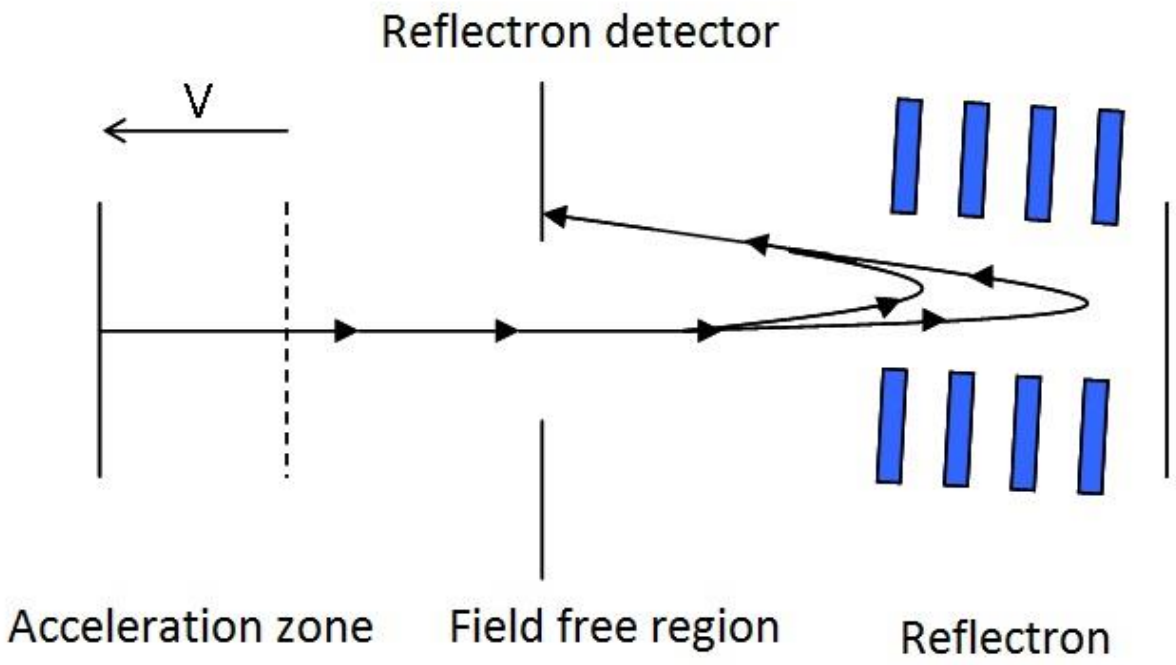

Figure 5: An illustration of a Time-of Flight detector with a reflectron. [36]

At TOF analyser is able to very rapidly measure single mass spectrums. This single spectrum can however have a very high background noise. Therefore, it is common to collect single spectrums over a short time period and combine them into a spectrum which will have much lower noise. For these experiments, this “scan duration” was set to 1 second and the delay between each scan was set to 0.1 second.

2.6 - The microchannel plates detector

A very common method to detect ions is the use of secondary electron multipliers (SEM). A tube made of a semiconductor is kept in a vacuum and ions are introduced to the tube. The SEM relies on the fact that when an energetic particle hits the surface of a metal or a semiconductor, secondary electrons are released through a process called secondary emission. The ions are introduced to the tube and collide with the wall, initiating secondary emission. The

emitted electrons may again collide with another wall in the tube, resulting in further secondary emission, creating more secondary electrons. This creates an avalanche of electrons, rapidly increasing the number of secondary electrons, which can be detected. By applying a positive potential that gradually increases trough the tube, the emitted electrons are pulled further into the tube by the attractive forces of the potential. In order to achieve a gradually increasing voltage throughout the tube the material used must have a sufficiently high resistance.

A channel electron multiplier (CEM) is a linear, heavily lead-doped glass tube, with its inside coated by a conductive layer of leadoxide, which is again coated by a layer of silicone dioxide. This construction allows the tube to withstand the high voltage applied to the tube (about 2 kV). A linear CEM is unstable at gains exceeding 10^4 due to an effect called ion-feedback. Residual gas becomes ionized during electronic ionization (EI), forming positive ions which become attracted to the inlet of the CEM tube, and generate random signals. When the tube is curved the gain increases to 10^8 due to a reduction in the free-path of the ions. This great increase in gain supresses the noise from the ion-feedback.

The microchannel plates (MCP) consists of millions of very tiny, linear CEMs. These CEMs are bundled together, forming a microchannel plate (MCP). To reduce the free-path of the ions and increase the gain, the channels are inclined a tiny bit from being perpendicular to the plate's surface. The gain of a single MCP is about 10^3-10^4, which is lower than a CEM and SEM, but by combining two MCPs together in such a way the inclined angles of the channels oppose each other, the gain is increased to 10^6-10^7. [32]

2.7 - Quantum chemistry

The topics covered here are well known and covered by most quantum chemistry courses and introductory books. This chapter will only cover the main parts of quantum chemistry theory. For the sources used here see the following references. [37-39]

2.7.1 - The Schrödinger equation

In classical mechanics, a system is described by the positions, masses, and forces acting on the different bodies in question. For this, Newton's laws are used to calculate how the system will evolve over time. In quantum mechanics, a system is described by a wave function and evolves over time following the Schrödinger equation. The Schrödinger equation was proposed by Erwin Schrödinger in 1926 and the general form (in one dimension) can be written as

$$H\Psi = E\Psi = i\hbar\frac{d\Psi}{dt} = -\frac{\hbar^2}{2m}\frac{d^2\Psi}{dx^2} + V(x)\Psi \qquad (21)$$

H is the Hamiltonian operator, Ψ is the wave function that is a function of both position and time, $\hbar$ is the Planck constant divided by 2π ($\frac{h}{2\pi}$), V(x) is the potential as a function of x and i is the imaginary number. By using the technique separation of variables, the time-independent Schrödinger equation can be derived and has the form

$$H\psi = E\psi = -\frac{\hbar^2}{2m}\frac{d^2\psi}{dx^2} + V(x)\psi \qquad (22)$$

Here, ψ is the wave function, but is only dependent on the position of the particle and E is the energy of the system. These equations can all be transformed to apply for all three dimensions, making the functions which are dependent on x to also be dependent on y and z coordinates as well and making the double derivatives also include the d^2/dy^2 and d^2/dz^2 derivatives as well. To simplify this derivative, the Laplacian operator can be used, which is simply the d^2/dx^2, d^2/dy^2 and d^2/dz^2 derivative and is symbolized by ∇^2.

2.7.2 - The Born-Oppenheimer approximation

The Hamiltonian operator for a system with N electrons and M nuclei can be separated into several terms (written in atomic units):

$$H = -\sum_{i=1}^{N}\frac{1}{2}\nabla_i^2 - \sum_{A=1}^{M}\frac{1}{2M_A}\nabla_A^2 - \sum_{i=1}^{N}\sum_{A=1}^{M}\frac{Z_A}{r_{iA}} + \sum_{i=1}^{N}\sum_{j>i}^{N}\frac{1}{r_{ij}} + \sum_{A=1}^{M}\sum_{B>A}^{M}\frac{Z_A Z_B}{R_{AB}} \quad (23)$$

Where i and j are specific electrons, M_A is the ratio of the mass of nucleus A to the mass of an electron, Z_A is the atomic number of nucleus A, r_{ij} is the distance between electron i and j, r_{iA} is the distance between electron i and nuclei A, R_{AB} is the distance between nuclei A and B and ∇^2 is the Laplacian operator. In this equation, the two first terms are the operators for the kinetic energy of the electrons and nuclei, respectively, the third term is the coulomb attraction between the electrons and the nuclei and finally the fourth and the fifth term represent the repulsion between the electrons and the nuclei, respectively.

A vital part of quantum chemistry is the Born-Oppenheimer approximation. Because the nuclei are much heavier than electrons and moves a lot slower, the Born-Oppenheimer approximation assumes the electrons are the only particles moving and the nuclei are static objects. Because the nuclei are considered as fixed bodies, their kinetic energy will be zero and the coulomb repulsion between the nuclei will be constant. If a constant is added to the expression in an operator, that constant is simply added to the operator eigenvalues and does not change the eigenfunctions. Therefore, both the second and fifth term of equation (23) (the terms for kinetic energy of the nuclei and the repulsion between them) can be removed from the operator and added to the result later. The remaining expression is called the electronic Hamiltonian:

$$H_{elec} = -\sum_{i=1}^{N}\frac{1}{2}\nabla_i^2 - \sum_{i=1}^{N}\sum_{A=1}^{M}\frac{Z_A}{r_{iA}} + \sum_{i=1}^{N}\sum_{j>i}^{N}\frac{1}{r_{ij}} \quad (24)$$

Because the system now considers the nuclei as fixed bodies, a new wave function can be made: one that depends explicitly on the coordinates of the electrons and parametrically on the coordinates of the nuclei.

$$\psi_{elec} = \psi_{elec}(\{r_i\};\{R_A\}) \tag{25}$$

The Schrödinger equation using the electric Hamiltonian and the electric wave function then becomes:

$$H_{elec}\psi_{elec} = \varepsilon_{elec}\psi_{elec} \tag{26}$$

In equation (26), ε_{elec} is the electronic energy. However, to get the total energy, the nuclear repulsion must also be included:

$$\varepsilon_{tot} = \varepsilon_{elec} + \sum_{A=1}^{M}\sum_{B>A}^{M}\frac{Z_A Z_B}{R_{AB}} \tag{27}$$

The main problem in quantum chemistry is to determine the electronic energy, however through the Born-Oppenheimer approximation; this has been simplified to being a value that relies only explicitly on the coordinates of the electrons and parametrically on the nuclei.

2.7.3 - The Hartree-Fock method

The first step in deriving the Hartree-Fock (HF) method is to properly describe the orbitals by a single determinant and ensuring the orbitals are the best approximation of the ground state for the N-electron system which is described by the electric Hamiltonian. The variation principle states that the best spin

orbitals must have a form which minimizes the electronic energy given by the expression in equation (28).

$$\begin{aligned} E_0 &= < \Psi_0 | H | \Psi_0 > \\ &= \sum_a < a|h|a > + \frac{1}{2} \sum_{ab} < ab||ab > \\ &= \sum_a < a|h|a > + \frac{1}{2} \sum_{ab} [aa|bb] - [ab|ba] \end{aligned} \tag{28}$$

In equation (28), <a|h|a> is the energy contribution of the kinetic and potential energy of electron a, [aa|bb] is the coulombic interaction between electron a and b, and [ab|ba] is the exchange interaction between electron a and b and Ψ_0 is the slater determinant for the ground state of the system. Because the last sums in the equation includes the interaction between a specific electron and all other electrons, every interaction is counted twice, which is the reason why the sum is multiplied by ½ to counteract this. The orbitals also have to be orthonormal, so adjusting the spin orbitals while keeping them orthonormal in order to obtain the lowest possible energy for the system will yield an equation that defines the best possible spin orbitals. This equation is called the Hartree-Fock integro-differential equation and has the form

$$\begin{aligned} h(1)\chi_a(1) + \sum_{b \neq a} \left[\int dx_2 |\chi_b(2)|^2 r_{12}^{-1} \right] \chi_a(1) \\ - \sum_{b \neq a} \left[\int dx_2 \chi_b^*(2) \chi_a(2) r_{12}^{-1} \right] \chi_b(1) = \varepsilon_a \chi_a(1) \end{aligned} \tag{29}$$

Where the first term is the kinetic and electron-nuclei attraction of electron 1, χ_a is spin orbital a, the first and second sums are the coulomb and exchange terms respectively and ε_a is the orbital energy for the spin orbital χ_a. From this equation an operator called the Fock-operator can be derived and has the form

$$f(1) = h(1) + \sum_b g_b(1) - K_b(1) \tag{30}$$

Equation (2) is the Fock-operator for electron 1, where g_b is the coulombic term and K_b is the exchange term in equation (19). The Fock-operator is used to describe the Hartree-Fock (HF) Hamiltonian, H_0, which is an approximate Hamiltonian that can be solved exactly for an N-electron system.

$$H_0 = \sum_{i=1}^{N} f(i) \tag{31}$$

By using the Hartree-Fock Hamiltonian on the slater-determinant for the ground state, the Hartree-Fock energy is found for the ground state of the system.

$$H_0|\Psi_0> = E_0^0|\Psi_0> \tag{32}$$

Where

$$E_0^{(0)} = \sum_a \varepsilon_a \tag{33}$$

This energy is not exact, but can be improved upon by perturbation.

2.7.4 - The self-consistent-field (SCF) procedure

In practice, the Fock-operator is used in the Roothaan equations (equation 27) to give the energy of the system.

$$FC = SC\varepsilon \tag{34}$$

Unfortunately, the last two sums in equation 23 depend on all the other electrons in the system. This problem can be simplified by finding the charge density matrix P of all the electrons, which turns out can be found by summing

up the charge contributions from all the electron wave functions, although it does not completely solve the problem of describing the location of the electrons. However by guessing a charge density matrix P, a guess of the position of the electrons can be made. This charge density matrix is then used to solve all the one-electron problems for the Fock-operator which allows for the determining of all the electron states in this density matrix. By using these new electron states, a new density matrix can be made, and the process is repeated. Each time the process is done, the energy is lowered, until the energy no longer change and the best estimate for the electron states and the lowest energy has been determined, which is in accordance with the variational principle. This process is called the self-consistent-field (SCF) procedure.

2.7.5 - Density functional theory

Density functional theory (DFT) takes on the same problem as HF-theory, but instead of using the wave functions of the electrons to compute the energy of the system, it uses the electron density. The Hoenberg-Kohn existence theorem states that a system with a specific electron density will only have one possible energy state. The second theorem Hoenberg and Kohn developed is the Hoenberg-Kohn variational theorem, which states that the charge density obeys the variational theorem. Because of these two theorems, DFT is considered to be an “exact” theory. Similarly to the HF-procedure, the initial electron is guessed and used to solve the Kohn-Sham equations which then give the means to calculate the occupied Kohn-Sham orbitals. These orbitals are then used to form a better electron density and the process is repeated in a SCF-manner until the electron density no longer changes.

However, while the exact energy of the system is a function of the density, the form of this function is unknown. Approximations to make an expression for the energy have been made, however this means that DFT with these approximations no longer are exact and does no longer necessarily obeys the variational principle; i.e. the energy can be lower than the exact answer. Various methods have been developed with DFT using different approximations that can generally be divided into groups depending on which

approximation that is applied to them. Such approximations can be the Local Density Approximation (LDA), General Gradient Approximation (GGA) or hybrid functions that adapt some terms from HF-theory (which gives rise to the popular B3LYP functional) to name a few of the approximations made to DFT.

2.7.6 - Basis sets

In order to carry out calculations on a molecule, the orbitals need to be represented mathematically. The wave function of the molecular orbital can be represented as a linear combination of N atomic orbital functions.

$$\phi = \sum_{i=1}^{N} \alpha_i \varphi_i \tag{35}$$

By squaring the wave function, the probability of finding an electron in a given position can be found, so it is preferable to use functions can simulate the "flexibility" of the electrons to move to positions that increases the electron density, but lowers the overall energy of the system. The greater amount of atomic orbital functions used in the linear combination, the closer the molecular orbital wave function described by this linear combination becomes to the exact wave function. The collection of functions (called basis functions) used is called a basis set. Unfortunately, due to practical limitations, a basis set with infinite amount of functions is impossible to achieve and a finite amount must be used instead. A larger basis set has more basis functions and results in longer calculation times. Larger systems also requires longer calculation times than a smaller system, so for a large system a smaller basis set may be chosen to prevent the calculation time from being too long. Sometimes special functions are needed to accurately describe a system. One example is systems with weakly bonded electrons which needs diffuse functions to describe those kinds of bonds.

The calculations used here use mostly the basis set aug-cc-pvtz; a Dunning's correlation consistent basis set. The pvtz indicates the basis uses triple-zeta (tz) functions for each valence atomic orbital, while a smaller basis set such as the pvdz uses a double zeta functions and a larger basis set such as the pvqz uses quadruple zeta functions. This kind of basis sets includes polarizing functions which is highly recommended when simulating an excited system. When the keyword aug- is added, diffuse functions are included to the basis set. Because the systems investigated here are anionic and have ligand effects, both diffuse and polarizing functions are needed in the calculations. 6-311+G**(d,p) is a smaller basis set than aug-cc-pvtz, but includes both diffuse and polarizable functions.

2.8 - Experimental details

2.8.1 - Collision gas inlet

An illustration of the gas inlet for the collision gas is shown in Figure 6. A sample of a volatile liquid is put in a vial and attached to the setup (the vial is shown on the left in the illustration). This setup allows the vapour from the liquid in the vial to be transported to the collision cell by opening valve A, E and the needle valve. If the pressure before the needle valve is not held constant, maintaining a stable and constant pressure in the collision cell may be difficult. By placing the sample vial in an ice bath will keep the temperature in the sample stable which will reduce the fluctuations of the vapour pressure as vapour pressure is dependent on temperature. Once the sample has been cooled to thermal equilibrium, valves A and D are opened while valve B, C and E are closed, allowing the gas vapour to flow through the tubes. Then, valve A is closed and valve B is opened, sealing the vial again and removing the gas in the tubes. This process is repeated and the pressure on the barometer is observed. When the barometer shows approximately the same pressure each time valve A is opened, the pressure experienced by the barometer will be largely due to the vapour pressure of the sample and not due to any air left in the vial when the vial was attached to the pipes. Before this liquid can be used as a collision

gas, it needs to be degassed, a procedure with will be described in the next section. Alternatively, by attaching a gas canister and opening valve C instead of valve A allows gas from the canister to be used as a collision gas. This is often used when the collision gas is an inert gas such as argon, which is commonly used in CID experiments. The pressure in the collision cell can be carefully controlled by adjusting the needle valve.

2.8.2 - Degassing procedure

During this procedure the needle valve is closed. The vial is placed in a container of liquid nitrogen until the liquid is frozen solid. Once the solution is completely frozen, the valves A, B are opened to pump out the gas within the pipes and vial for 10-30 minutes. After this time has passed, valve A is closed and a water-bath is placed around the vial to thaw the sample. As the sample thaws, gas trapped in the liquid is released and can be seen in the form of bobbles forming in the sample and rising to the surface during the thawing process. Once the sample has thawed completely, the sample is frozen again using liquid nitrogen and the procedure is repeated again. This cycle is repeated until no more bobbles are observed during the thawing and it should be done a minimum of 3 times before using the sample for experiments.

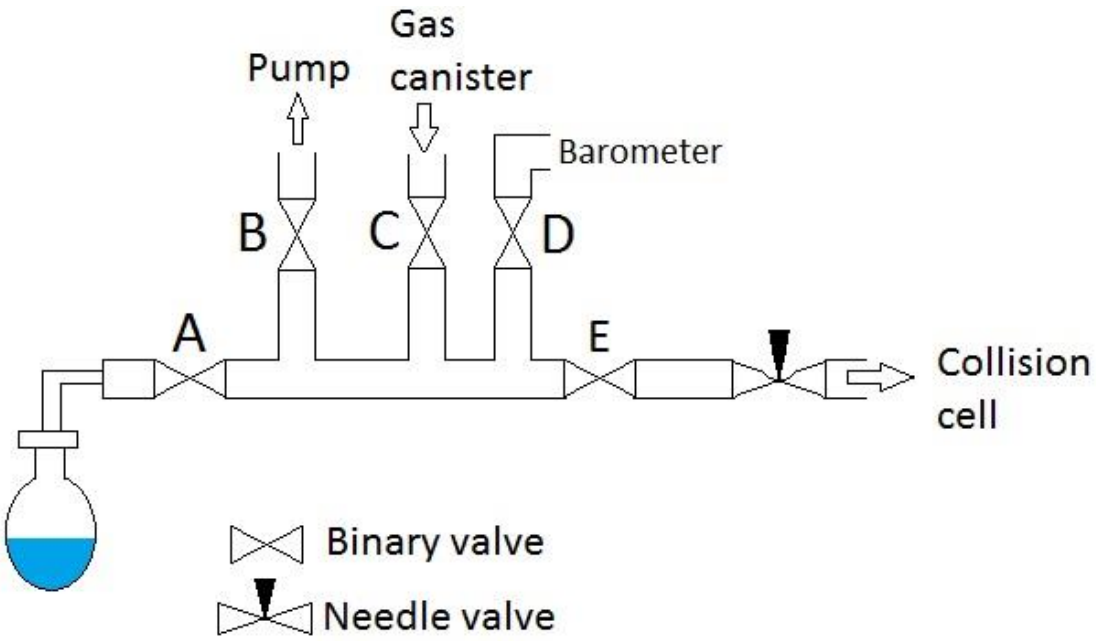

Figure 6: Illustration of the gas inlet for the collision cell in the QTOF-MS.

Figure 7: Picture of the gas inlet on the QTOF-MS. The vial placed in the ice bath is shown on the right in the picture.

2.8.3 - Experimental setup

The ions were produced using ESI, with nitrogen being used as the nebulizer gas. By introducing water (HiPerSolv Chromanorm for HPLC) to the ESI under atmospheric pressure, oxygen molecules were ionized into superoxide. Due to the presence of water, superoxide is also can also become hydrated, causing the formation of water clusters ($O_2^{\bullet -}(H_2O)_n$) of varying sizes (n). [18] By using the quadrupole to only accept a certain m/z value, a cluster with a specific value of n was able to pass through it to then be guided by a hexapole into a collision cell. The model chemicals were introduced to the collision cell through a gas inlet (see section 2.8.1) and in this collision cell the water clusters reacted with the model chemicals. The products and unreacted clusters then exited the collision cell and entered a time-of-flight mass analyser. The scan duration was set to 1 second and the delay between each scan was set to 0.1 second.

In a QTOF-MS, the background noise may occur from various sources such as electrical noise from the instrument. The signal-to-noise ratio (S/N) is used to describe the uncertainty of a measured intensity in a mass spectrum. Noise is

random and will therefore be statistical in nature, and can therefore be reduced by increasing the measurement time or increasing the duration of each scan. For a single scan, the background noise is 1-2 at a random m/z value and the chance of this noise to occur at the same m/z value twice is rather low, though with increased measurement times it may occur once or twice. By ensuring the measurement time is long enough to give the products in the combined spectra at least 1000 counts of a product, a S/N > 10^3 is possible. This can be achieved by having a measurement time that depends on the signal of the precursor ion; if the intensity of a precursor ion (i.e. the superoxide water cluster) is 11 counts/scan, using a measurement time of 10 minutes will give a total of 6000 counts for that ion in the combined spectra. Similar approximate guidelines for other intensities are given in Table 1.

Table 1: Overview of the approximate guidelines for determining the duration length of a measurement based on the average signal strength of the molecular ion.

Counts/scan	Recommended measurement duration
10 ≥	15-25 mins
11-20	10 mins
21-40	8 mins
41-90	5 mins
91-350	2 mins

Measurements were conducted to investigate the effects the cluster size n, collision energy E_{com} and collision cell pressure P_{cell} had on the reactions. Before the measurements were started, the position of the capillary needle of the ESI was adjusted to increase the signal of the ions as much as possible. The adjustments had to be very carefully applied and constantly monitored; the optimal position for the needle would often be very close to the inlet to the MS. However, if the needle got too close to the inlet an electric discharge could occur between the needle and the inlet, potentially damaging the ESI or disrupt the computer system of the QTOF-MS. For each measurement, the capillary voltage and cone voltage in the ESI was adjusted to give a maximum signal for the water cluster anion, although 350 counts/scan was the maximum desired value; higher signal than this could decrease the lifetime of the microchannel plates detector. The capillary voltage was adjusted between 2.90 kV and 3.30 kV the cone voltage was adjusted between 3V and 95V. Depending on what

cluster size (n) was being used, the optimal value for these parameters could vary greatly. Desolvation gas seemed to have a negative effect on the production of the clusters when pure water was used as the solvent. Reference measurements were taken in between sets of measurements to ensure the signal was stable. For these measurements a cluster size n = 2 was used at a collision energy of E_{com} = 1.0 eV because this cluster had the highest production of all the other clusters at this collision energy. Although in some special cases, naked superoxide (n = 0) cluster was used instead.

Of all the water clusters used, the naked superoxide anion (n = 0) was the most difficult anion to produce (1-5 counts/scan). This low production of superoxide and the ease at which the n = 1 - 4 clusters are produced, indicates that superoxide has a high affinity towards water and will easily form a water cluster if in the presence of water. Because methanol vaporizes more easily than water it is possible that superoxide has a lower affinity towards methanol while still being able form superoxide in the electrospray. In an effort to improve the production of this ion, an experiment with methanol and no collision gas was done. These results were compared to a similar experiment done with water. When compared the results, despite the low production using water the experiments with methanol yielded an even lower production of the naked superoxide anion. However, when using a 50/50 solution of water/methanol along with turning on the desolvation gas, the production of the n = 0 cluster is significantly increased. Because this was discovered later in the project, not all measurements used this technique for the production of the n = 0 cluster.

Quantum chemical calculations were conducted using DFT with the B3LYP functional and aug-cc-pvtz as the basis set. For larger systems, the basis set 6-311+G**(d,p) was first used to optimize the geometry before the aug-cc-pvtz basis set was used to fine-tune the geometry and energy optimizations. The reason for this choice of functional and basis set is because it tends to give a more accurate estimate of the energies than smaller basis sets such as the 6-311+G**(d,p) basis set and the systems are relatively small, making computation times using this large basis set manageable. The B3LYP functional was used as it seems to provide good results for complexes formed in the gas-phase from S_N2 reactions. It is important to note however that B3LYP does tend

to underestimate energy barriers when compared to other methods and experimental data. [40]

A paper was published by M. Arshadi and P. Kebarle in 1970, reporting the enthalpies of the hydration reaction of superoxide for the cluster sizes n = 1, 2, 3. [41] The enthalpies reported in this paper have been compared to those found using B3LYP/aug-cc-pvtz and the comparison is shown in Table 2.

Table 2: The hydration enthalpies of superoxide. The experimental values determined compared to the values determined by using calculations using the B3LYP method with the cc-aug-pvtz basis set.

$O_2^{\bullet-}(H_2O)_{n-1} + H_2O \rightarrow O_2^{\bullet-}(H_2O)_n$	Experimental (kJ/mol)	B3LYP (kJ/mol)	Difference (kJ/mol)
n = 1	-77.0	-78.6	-1.6
n = 2	-72.0	-60.1	11.9
n = 3	-64.4	-51.9	12.5

The difference between the experimental values and the calculated ones using B3LYP/aug-cc-pvtz are relatively small, which shows that B3LYP/aug-cc-pvtz is a good method to use for calculating the energies of small superoxide water clusters. This small energy difference could be due to B3LYP not being able to compute the exact energy of the system, the experimental value is slightly inaccurate, or a combination of both.

Previous publications using B3LYP on small sulphur systems similar to the dimethyl disulphide (DMDS) system that was investigated here report that this functional does not perform poorly on such systems, but better methods exist. [34, 42] Since B3LYP seems to accurately predict the trend of hydration of superoxide and it performs decently on DMDS systems, B3LYP became the functional of choice for this paper.

2.8.4 - Execution of experiments involving dimethyl disulphide

The first sets of experiments were conducted using dimethyl disulphide as the collision gas. About 2.5 mL of 99% pure dimethyl disulphide (from Sigma Aldrich) was added to a vial which was then attached to the gas described in section 2.8.1, which then introduced the vapours from the sample to the

collision cell. Superoxide water clusters were produced in the electrospray and transported into and through the collision cell where collisions between the water clusters and DMDS would occur. An attempt to keep the pressure in the collision cell was made by keeping the vial of DMDS in an ice bath. For the first two experiments, the pressure in the collision cell gradually increased as time progressed, but the experiments after this the pressure was kept at about the same value (during experiment the average pressure was $2.15 \bullet 10^{-4}$ a standard deviation of $\pm 5 \bullet 10^{-5}$ mBar, the relative standard deviation was 5.1%). These experiments were however more qualitative and the slight change in pressure in the early experiments would not affect the results to any great degree.

Measurements were done for various collision energies (0.4, 0.6, 0.9, 1.0, 2.0, 5.0 eV) and various water cluster sizes (n = 0, 1, 2, 3, 4). Increasing the pressure does seem to increase the production of $O_2^{\bullet -}$(DMDS), but no quantitative investigation were done on this due to the relatively low signal of the adducts and products observed.

Quantum chemical calculations were done on the species observed as well as some hypothesised products. These calculations were carried out using density functional theory (B3LYP) with the aug-cc-pvtz basis set. Transition state calculations were done by first performing a scan along the reaction coordinate using the keyword Modredundant and performing a transition state calculation in the energy maxima found on the energy profile.

2.8.5 - Execution of experiments involving acetic acid

As with DMDS, experiments were done using acetic acid as the collision gas in the collision cell. About 2.5 mL of acetic acid (100% extra pure from Sigma-Aldrich) was added to a vial and attached to the gas inlet. Water clusters of varying sizes were then produced in the electrospray, mass selected in the quadrupole and introduced to the collision cell where collisions with acetic acid molecules could occur before the m/z of the ions could be analyzed and detected by the TOF-detector.

Measurements were carried out at collision energies of 0.6, 0.9, 1.0, 1.3 and 1.7 eV. As with experiments with DMDS, water clusters of the sizes n = 0, 1, 2, 3, 4 were used as well. In addition, the effect of the pressure had a great effect on product formation, so a qualitative investigation of this was done as well. The collision cell pressures investigated were $1.00 \bullet 10^{-5}$ mBar, $1.80 \bullet 10^{-4}$ mBar, $2.50 \bullet 10^{-4}$ mBar, $3.30 \bullet 10^{-4}$ mBar and $4.00 \bullet 10^{-4}$ mBar. The collision cell pressure was recorded each time a measurement was started and analysis showed the pressure was relatively stable when the vial of acetic acid was cooled in an ice bath ($\pm 1 \bullet 10^{-5}$ mBar at most).

The energies of the hypothesized and observed species were calculated using DFT (mainly using B3LYP functional with the aug-cc-pvtz basis set, but 6-311+G**(d,p) basis set was used for rough geometry optimization for larger system before aug-cc-pvtz was used to fine tune the geometry and energy optimizations). Larger water clusters tend for have more than one stable conformer so the energy of several conformations was calculated and the most stable ones were used.

3. Results

3.1 - Relative abundance

When comparing the intensities of peaks in a mass spectra and analysing reaction ratios, it is useful to report the peaks in their relative abundances (RA). In a normal mass spectrum, the intensity of each peak is measured in the total amount of counts that was collected for that m/z value during the measurement. By removing the peaks of the background noise and summing the counts of the remaining peaks, the total amount of counts is found. To obtain the relative abundance of an ion, the counts of its peak (I_i) is multiplied by 100 and divided by the total amount of counts in the spectrum (eq. (36)).

$$RA_i = \frac{I_i * 100}{\sum_j I_j} \tag{36}$$

The relative abundance is reported in %. Using relative abundances allows one to easily distinguish products whose formations are more favourable or less favourable, regardless of the measurement time. This method is useful when discussing the reactivity of a system.

3.2 - Dimethyl disulphide

3.2.1 - n = 0

Figure 8 shows the spectrum where DMDS is used as the collision gas and the naked superoxide anion radical ($O_2^{\bullet -}$, m/z = 31.99) is the molecular ion. In this spectrum, no other significant peaks are observed besides the one for the molecular ion. As the collision energy was increased, some smaller peaks were observed, however no conclusions could be drawn from these peaks as their intensities were too low (<0.1% of the abundance of the molecular ion).

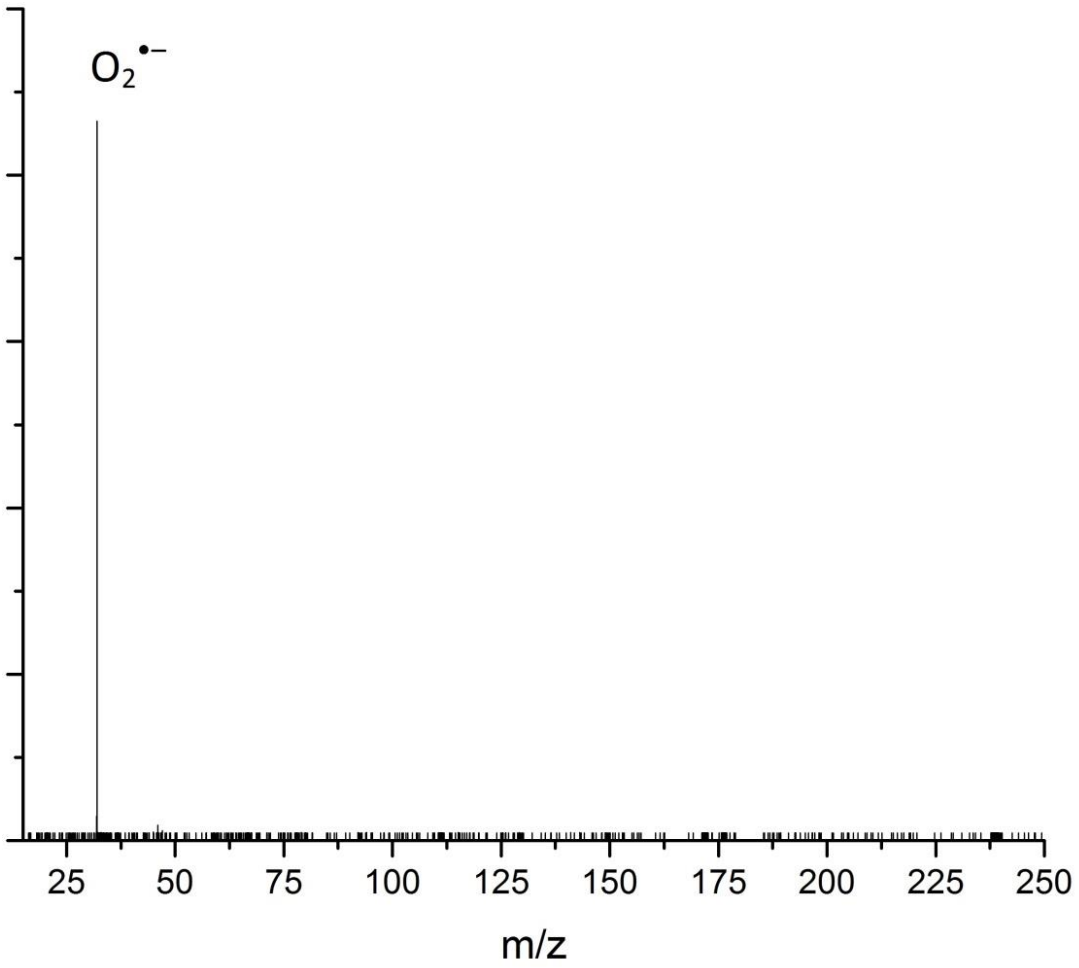

Figure 8: Spectrum taken by using naked superoxide as molecular ion with a E_{com} = 0.6 eV and DMDS as collision gas with a pressure of 2.18E-4 mBar. The spectrum shows no significant reaction under these conditions.

3.2.2 - n = 1

When the n = 1 water cluster ($O_2^{\bullet-}(H_2O)$), m/z = 50.00) is the molecular ion, a single peak is observed at m/z = 126, which is a match for $O_2^{\bullet-}$(DMDS), as shown in Figure 9. The reaction is observed with the collision energies 0.6 eV, 1.0 eV and 2.0 eV, but the signal is the strongest when 1.0 eV is used. The relative abundance of this peak is low (about 2.5% relative abundance at E_{com} = 1.0 eV), as indicated in the figure. An illustration of the geometry for this adduct is shown in Figure 10.

The formation of this adduct is accompanied by the loss of a water molecule from the cluster, indicating the reaction is exothermic. Because the system is

adiabatic, the excess energy makes the adduct unstable and the loss of a water molecule gives the adduct a way to release energy and become stabilized.

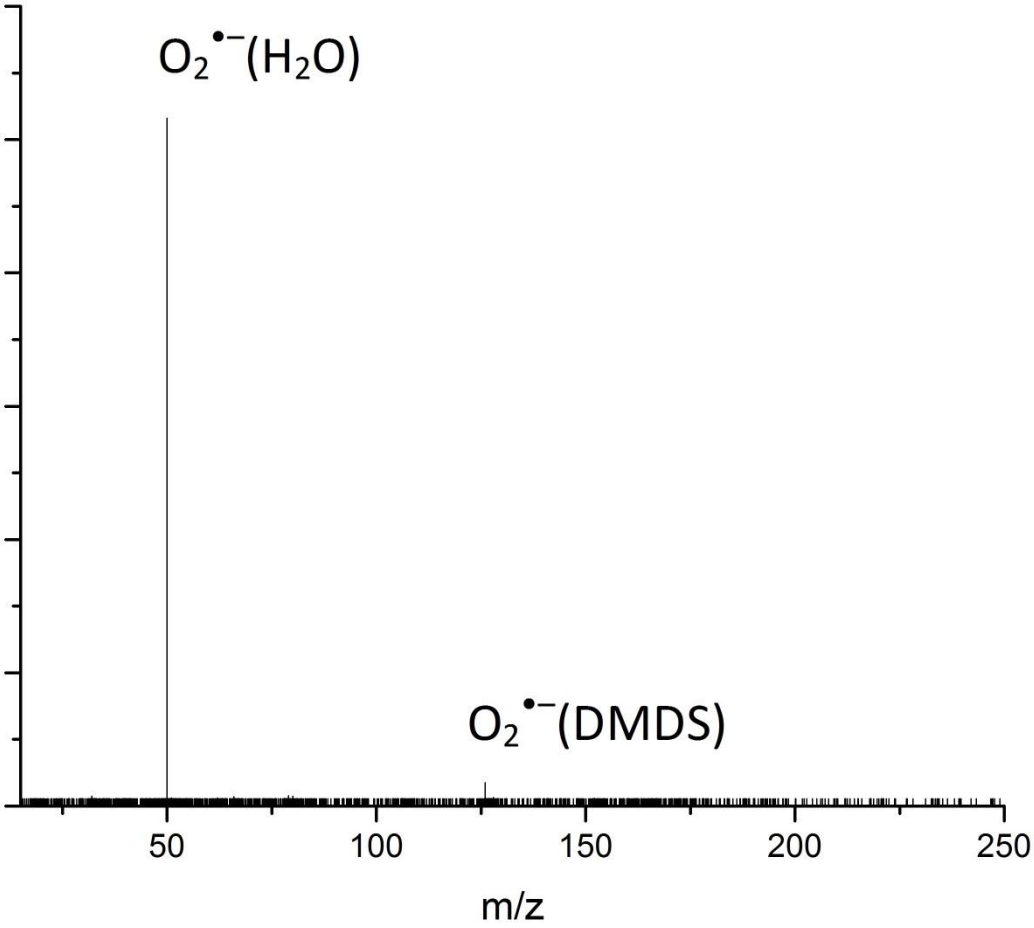

Figure 9: Spectrum taken by using $O_2^{\bullet-}(H_2O)$ cluster as molecular ion with E_{com} = 1.0 eV and DMDS as collision gas with a pressure of 2.20E-4 mBar. DMDS forms an adduct with the water cluster $O_2^{\bullet-}$(DMDS) while vaporizing the water molecule.

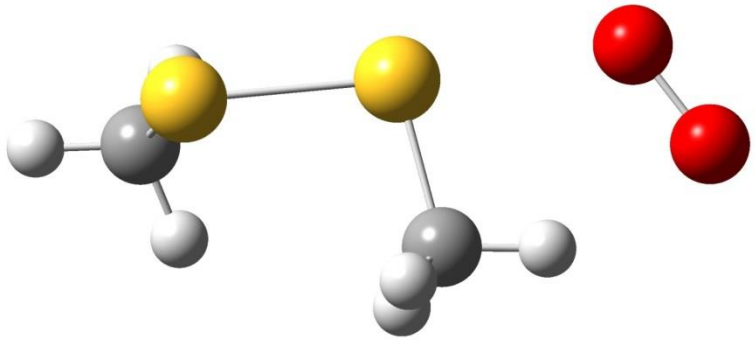

Figure 10: Illustration of the structure of the $O_2^{\bullet-}$(DMDS) adduct. The structure was optimized using the B3LYP functional and the aug-cc-pvtz basis set. The most stable conformation has the superoxide almost coaxial to the S-S bond.

3.2.3 - n = 2

If the n = 2 water clusters ($O_2^{\bullet-}(H_2O)_2$), m/z = 68.03) is used as the molecular ion, a peak at m/z = 144 is observed, which is a match with the $O_2^{\bullet-}(H_2O)$(DMDS) adduct (see Figure 11). Again, the formation of this adduct is accompanied by the loss of a water molecule, indicating the reaction is exothermic.

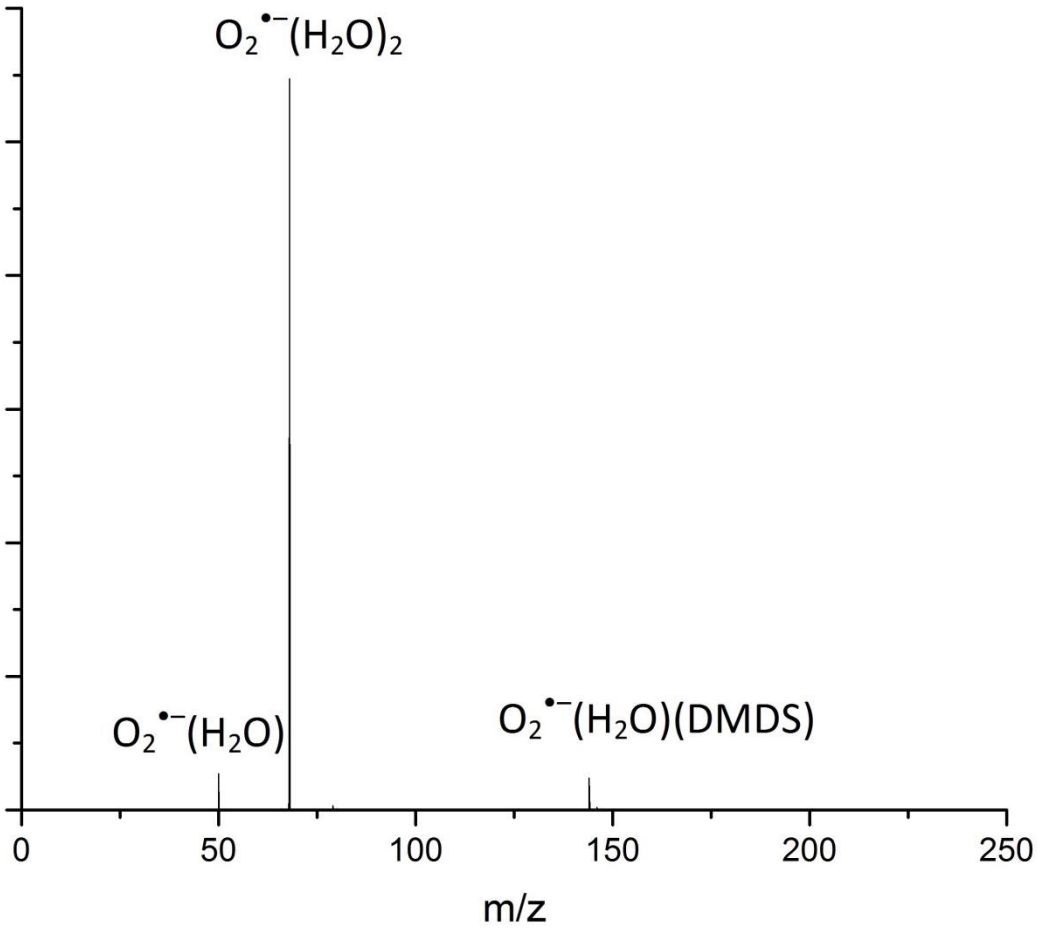

Figure 11: Spectrum taken by using $O_2^{\bullet-}(H_2O)_2$ cluster as molecular ion with E_{com} = 1.0 eV and DMDS as collision gas with a pressure of 2.20E-4 mBar. DMDS forms an adduct with the water cluster $O_2^{\bullet-}$ (H_2O)(DMDS) while vaporizing the water molecule.

When E_{com} was increased, a peak corresponding to $O_2^{\bullet-}$(DMDS) was observed as well. As E_{com} gradually increased, the peak intensity of $O_2^{\bullet-}$(DMDS) increased while $O_2^{\bullet-}(H_2O)$(DMDS) decreased. An example of this is shown Figure 12; when E_{com} = 1.0 eV, the intensity of the peak for $O_2^{\bullet-}(H_2O)$(DMDS) is stronger than the peak for $O_2^{\bullet-}$(DMDS) (figure a), when the collision energy increased to 2.0 eV, the peak for $O_2^{\bullet-}$(DMDS) is stronger than the peak for $O_2^{\bullet-}(H_2O)$(DMDS) (figure b). It should also be noted that the counts of both peaks are significantly lower

when the collision energy is 2.0 eV compared to when the collision energy is 1.0eV. At E_{com} = 5.0 eV, the signal of both peaks were almost completely gone, only a small trace of $O_2^{\bullet-}$(DMDS) was observed.

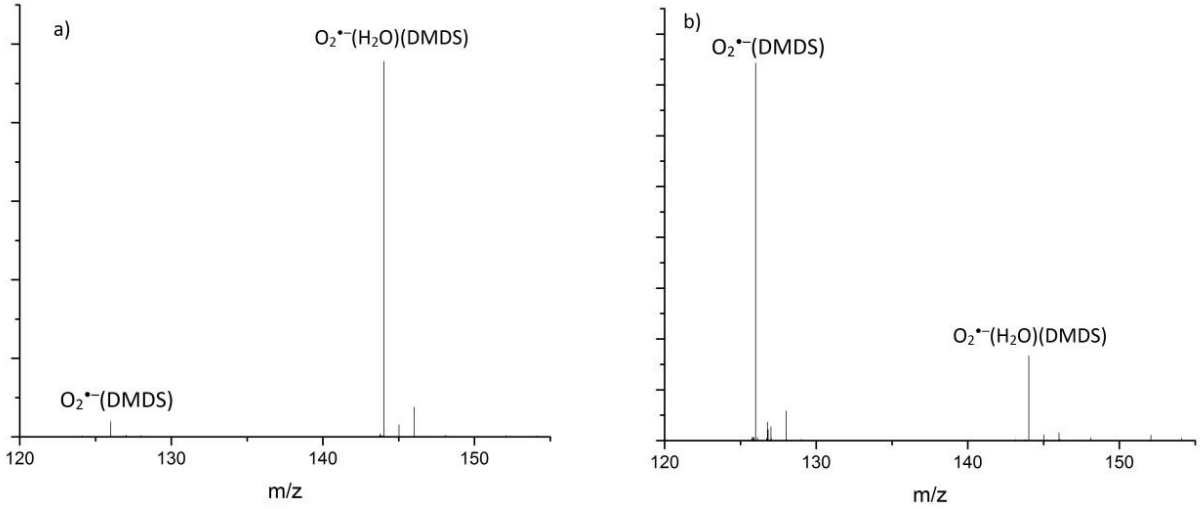

Figure 12: Comparison of two spectras in the interval m/z = 120 to 155. In both spectras the $O_2^{\bullet-}(H_2O)_2$ cluster was used as the molecular ion and the pressure of DMDS in the collision cell was 2.20E-4 mBar. In figure a) the collision energy E_{com} was 1.0 eV. In this figure, the $O_2^{\bullet-}$ (H_2O)(DMDS) at m/z = 144 is the dominating peak. In figure b), E_{com} was increased to 2.0eV. This caused $O_2^{\bullet-}$(DMDS) at m/z = 126 to become the peak with the highest intensity.

3.2.4 - n = 3, 4

The same trend is observed for the n = 3, 4 clusters; at low collision energies (E_{com} = 0.6 eV, 1.0 eV) adducts with the loss of one or two water molecules is observed, when the collision energy is increased to 2.0 eV the loss of two and three water molecules are observed and at 5.0 eV the loss of all water molecules are observed.

The adduct formations observed to follow this general reaction:

$$O_2^{\bullet-}(H_2O)_n + DMDS \rightarrow O_2^{\bullet-}(H_2O)_{n-x}(DMDS) + xH_2O \qquad (37)$$

Where n ≥ x ≥ 1. At lower collision energies the following reaction x = 1, but as this energy increases, so does the value of x. The trends that were observed are shown in in Figure 13 through Figure 15.

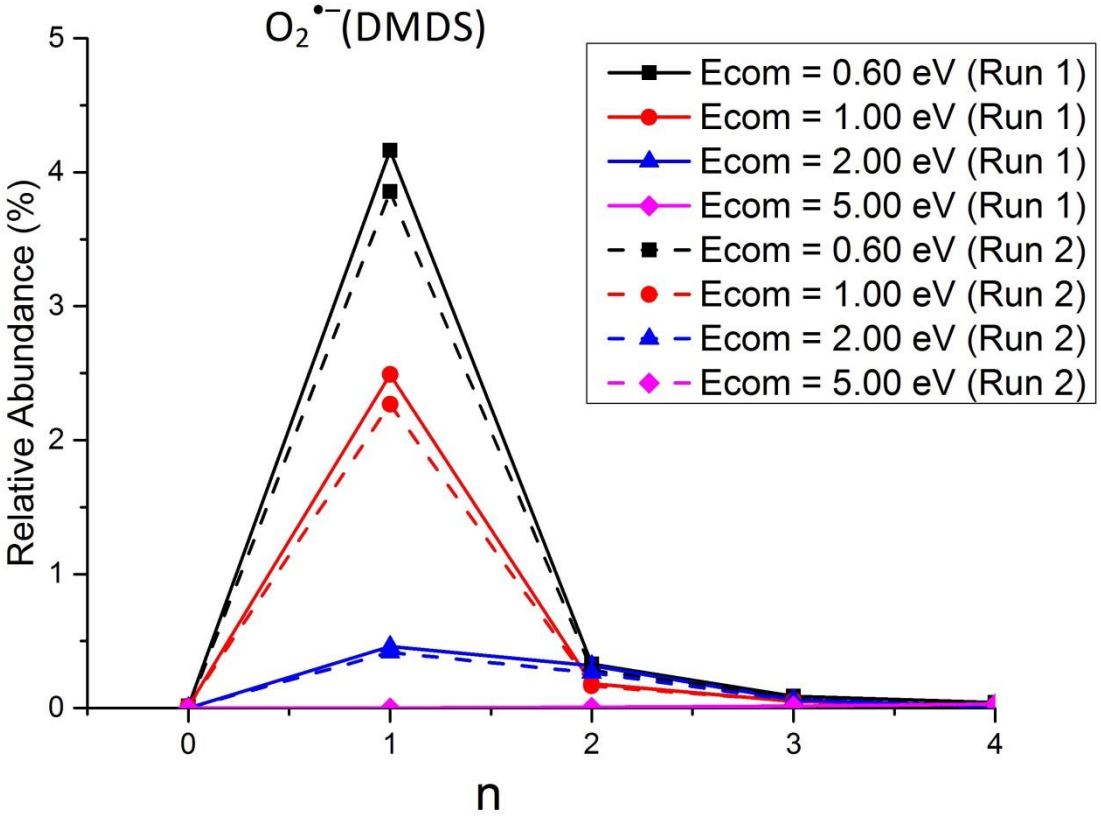

Figure 13: The relative abundance of the $O_2^{\bullet-}$(DMDS)-adduct at various collision energies plotted against the water cluster $O_2^{\bullet-}(H_2O)_n$, n = 0-4. The equation for this reaction is $O_2^{\bullet-}(H_2O)_n + DMDS \rightarrow O_2^{\bullet-}(DMDS) + nH_2O$. The pressure of DMDS in the collision cell used for these measurements was approximately 2.20E-4 mBar. There is a clear increase in the formation of this adduct when a cluster of $O_2^{\bullet-}(H_2O)$ is used.

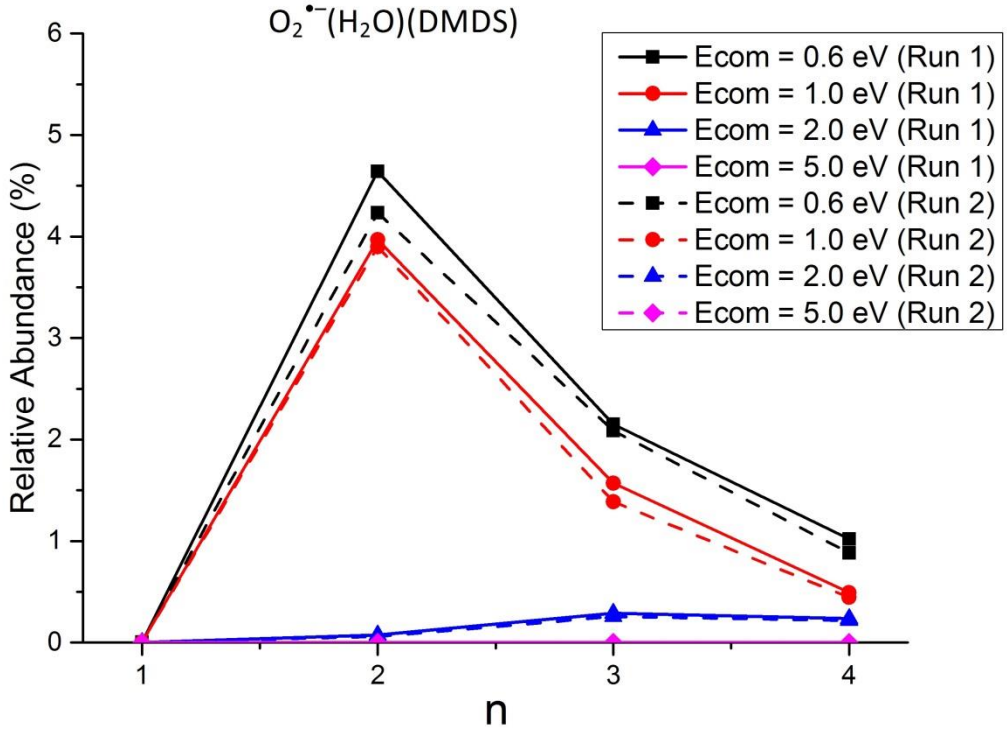

Figure 14: The relative abundance of the $O_2^{\bullet-}(H_2O)$(DMDS)-adduct at various collision energies plotted against the water cluster $O_2^{\bullet-}(H_2O)_n$n = 1-4. The equation for this reaction is $O_2^{\bullet-}(H_2O)_n + DMDS \rightarrow O_2^{\bullet-}(H_2O)(DMDS) + (n-1)H_2O$. The pressure used for these measurements was approximately 2.20E-4 mBar. There is no such reaction at n = 1, a maxima at n = 1 and the relative abundance decreases when n increases beyond this point.

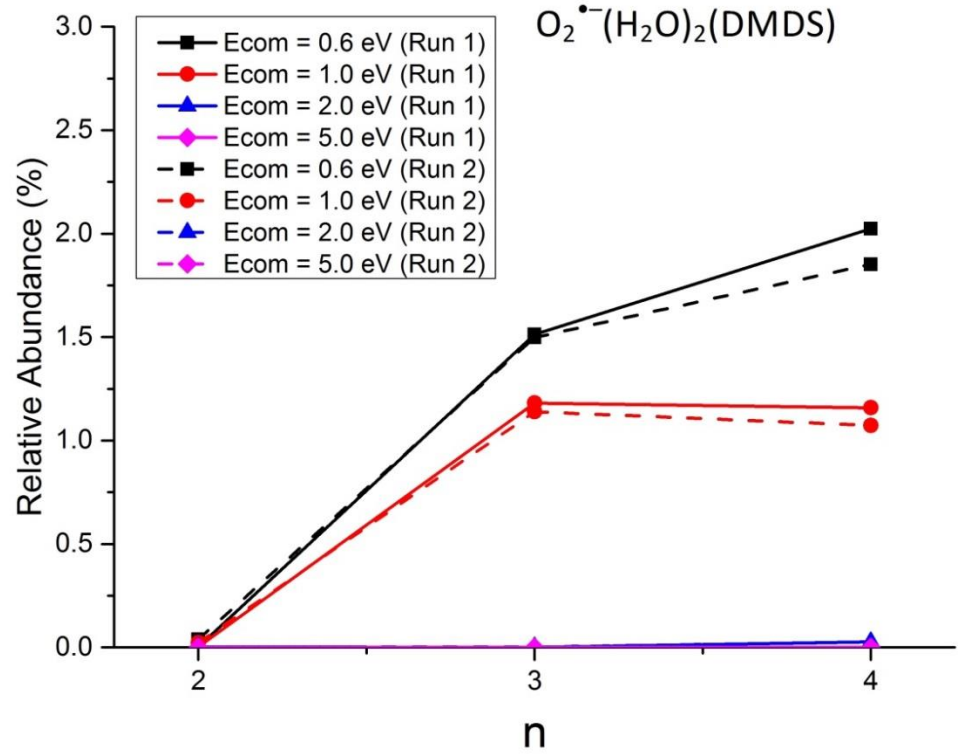

Figure 15: The relative abundance of the $O_2^{\bullet-}(H_2O)_2$(DMDS)-adduct at various collision energies plotted against the water cluster $O_2^{\bullet-}(H_2O)_n$n = 1-4. The equation for this reaction is $O_2^{\bullet-}(H_2O)_n + DMDS \rightarrow O_2^{\bullet-}(H_2O)_2(DMDS) + (n-2)H_2O$. The pressure of DMDS in the collision cell used for these measurements was approximately 2.20E-4 mBar. This reacton was only observed when n ≥ 3.

3.2.5 - Bond cleavage investigation

Two peaks with very low relative abundances were observed at m/z = 47 and m/z = 79 and could the result of a cleavage of the S-S bond. For this system, several molecular compositions match these m/z values. The suggested molecular compositions for m/z = 47 are CH_3S^- and $CH_3O_2^-$ while the suggested molecular compositions for m/z = 79 are $CH_3SO_2^-$ and CH_3SS^-. A high-resolution spectrum was taken; using the water clusters and adducts to calibrate the instrument. The results are shown in Table 3 and Table 4. Neither of the suggested molecular compositions for m/z = 79 are a match and could be the result of poor calibration in this region. During these measurements, a peak with a higher intensity was observed at m/z = 80 and is a good match for $CH_3SO_2H^-$ (Table 4), the mechanism for this reaction is unknown. Due to the unknown neutral products of this reaction, an energy diagram cannot be made for the formation of this product. CH_3S^- is a good match for m/z = 47. The isotope pattern of these species could not be used in determining the structure as small signals appeared at every integer m/z value in this region, which could be due to contamination. Due to the low intensities of these species, no certain conclusion can be drawn.

Table 3: High-resolution masses of CH_3SO_2, CH_3S_2 and the observed peak in this area. None of the suggested molecules is a good match with the observed mass.

Compound	m/z
Observed m/z = 79 peak	79.008
$CH_3SO_2^-$	78.968
CH_3SS^-	78.985

Table 4: High-resolution masses of CH_3O_2, CH_3S and the observed peak in this area. The observed mass is a good with the CH_3S^-.

Compound	m/z
Observed	46.998
$CH_3O_2^-$	47.013
CH_3S^-	46.996

Table 5: Comparison of the observed mass at m/z = 80 and the monoisotopic mass of $CH_3SO_2H^-$. The observed peak is a good match with this molecular composition.

Compound	m/z
Observed	79.992
$CH_3SO_2H^-$	79.993

These low intensities may be explained by the energy diagram for these species, which will be shown and discussed in section 3.4.2.

3.3 - Acetic acid

The three parameters investigated (cluster size, collision energy and pressure) with this system and each seemed to have a great effect on the reactions occurring and their effects will be mentioned separately.

3.3.1 - Cluster size (n)

Cluster size clearly had a great impact on the formation of the various products. When the naked superoxide anion (n = 0) was used as the molecular ion, deprotonation of acetic acid (m/z = 59) was observed. If a $O_2^{\bullet-}(H_2O)_n$ cluster with n = 1 - 4 is the molecular ion however, the signal from deprotonated acetic acid is strongly reduced and adducts of the water cluster and acetic acid were observed. This is illustrated in Figure 16.

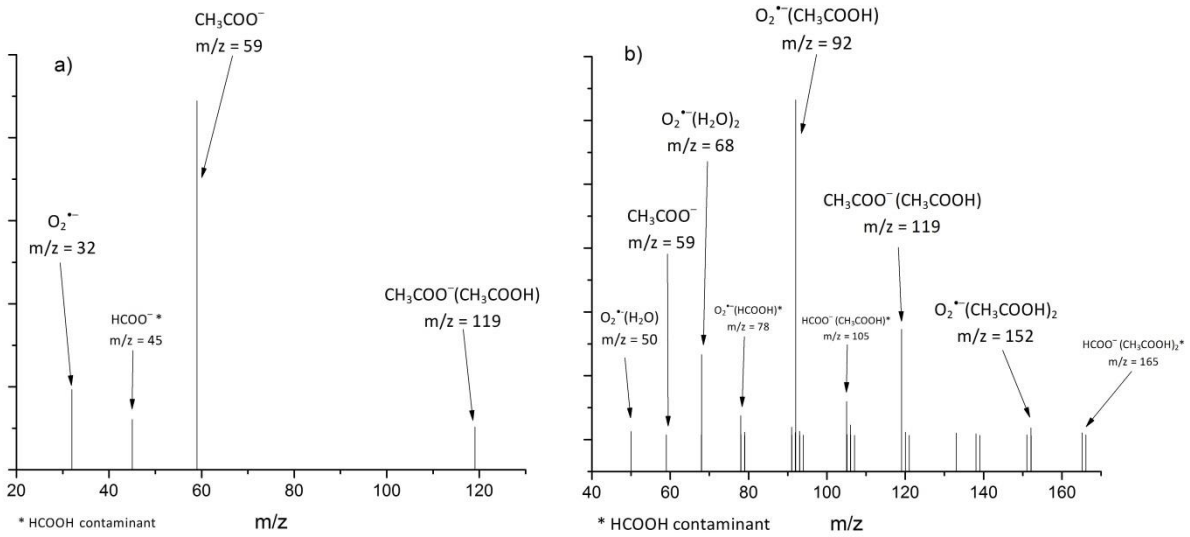

Figure 16: Comparison of two spectra. For both measurements, the collision energy E_{com} was set to 0.9 eV and the pressure of CH_3COOH in the collision cell was 3.30E-4 mBar. In spectra a, $O_2^{\bullet-}$ ions were used. In this spectra deprotonated acetic acid was observed as well as a dimer at m/z = 119. In spectra b, $O_2^{\bullet-}(H_2O)_2$ cluster was used. When this cluster was used, several adducts were observed while the signals from deprotonated acetid acid is severly reduced. Some smaller peaks from HCOOH contamination from a previous experiment were also observed.

Figure 17 shows how the peak of $O_2^{\bullet-}(CH_3COOH)$ (m/z = 92) is dependent on the cluster size of the molecular ion. While this peak is not observed when the cluster n = 0 is used as the molecular ion, it is very dominant when the n = 2 cluster is used.

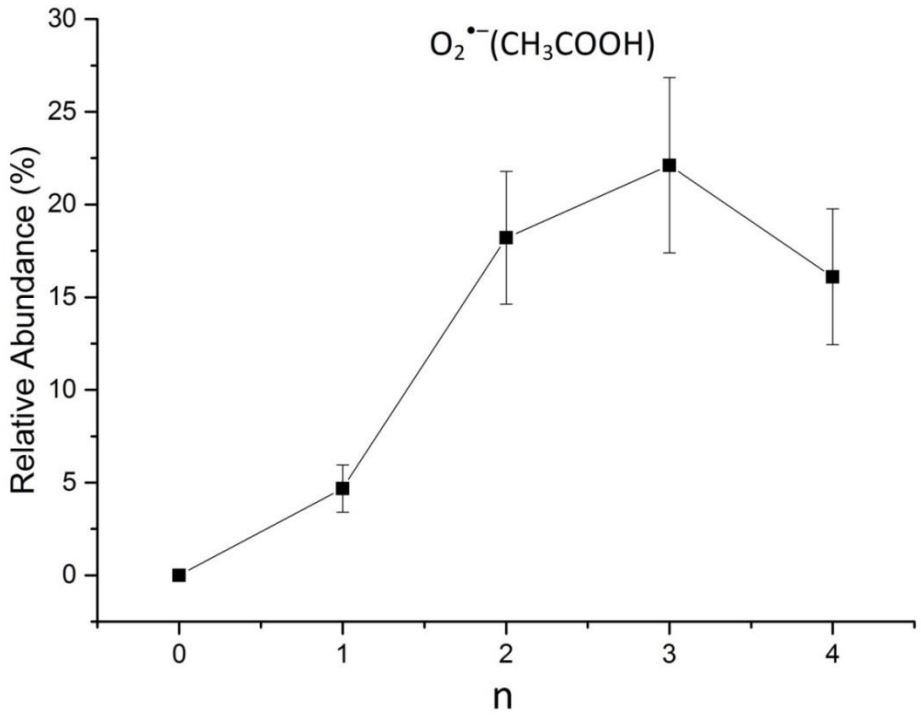

Figure 17: Plot of the relative abundance for the peak for the reaction $O_2^{\bullet-}(H_2O)_n + CH_3COOH \rightarrow O_2^{\bullet-}(CH_3COOH) + nH_2O$ as a function of the cluster size, n. For these measurements the pressure of CH_3COOH in the collision cell was 2.50E-4 mBar and E_{com} was set to 1.3 eV. The reaction becomes more favourable as n increases until n = 3 and then decreases when n = 4. No reaction is observed when n = 0.

The $O_2^{\bullet-}(CH_3COOH)$ adduct is only observed together with the loss of at least one water molecule. As seen in Figure 16a, none of this adduct is observed when n = 0 is used, but when n = 1 is used, no $O_2^{\bullet-}(H_2O)(CH_3COOH)$ (m/z = 110) is observed. The same trend is observed for other cluster sizes as well. The trend can be explained by the reaction

$$O_2^{\bullet-}(H_2O)_n + CH_3COOH \rightarrow O_2^{\bullet-}(H_2O)_{n-m}(CH_3COOH) + mH_2O \quad (38)$$

where n ≥ m ≥ 1. On the other hand, the relative abundance of CH_3COO^- rapidly declines as the cluster size is increased and when two to four water molecules are present, the signal disappears completely. This trend is shown in Figure 18 and the reaction equation for this product is described in equation (39).

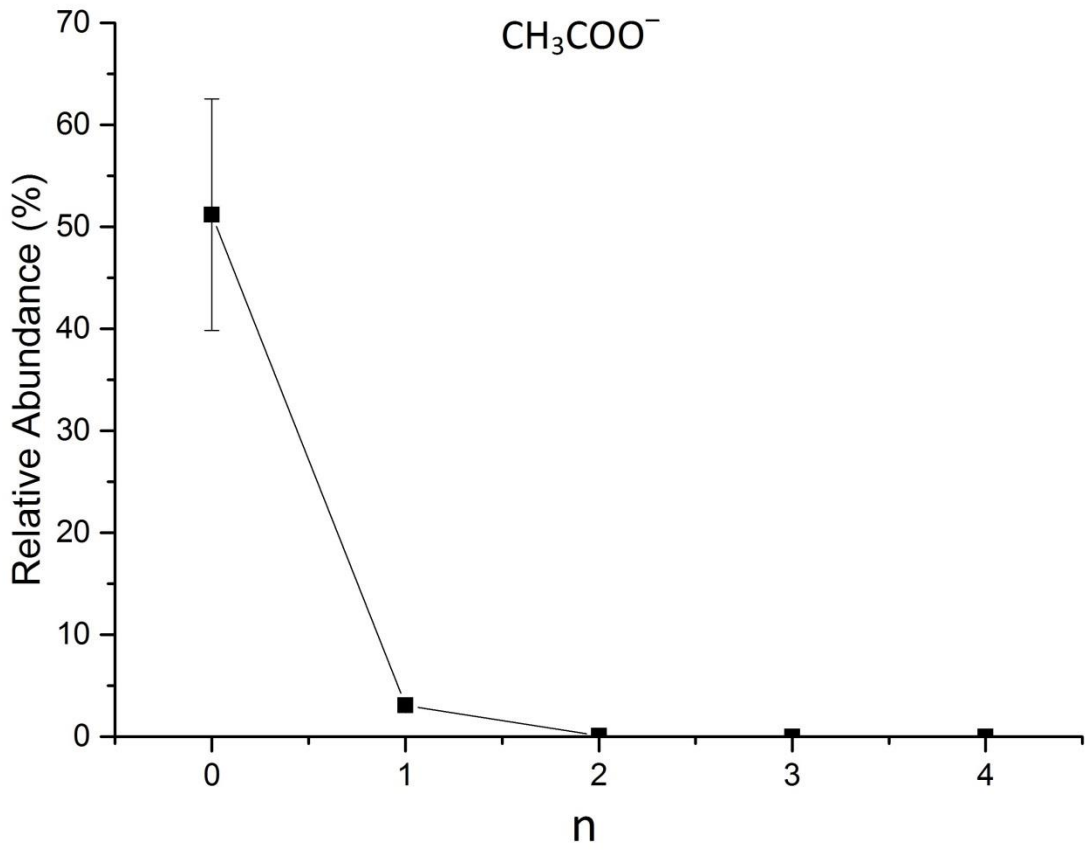

Figure 18: Plot of the relative abundance for the peak for the reaction $O_2^{\bullet-}(H_2O)_n + CH_3COOH \rightarrow CH_3COO^- + OOH^{\bullet} + nH_2O$ as a function of the cluster size, n. For these measurements the collision cell pressure was 2.50E-4 mBar and E_{com} was set to 0.6 eV.

$$O_2^{\bullet-}(H_2O)_n + CH_3COOH \rightarrow CH_3COO^- + OOH^\bullet + nH_2O \qquad (39)$$

3.3.2 - Collision energy (E_{com})

As the center-of-mass energy was increased, the abundance of various products was increased while some decreased. In particular, reactions that involved the loss of more water molecules were more dominant at higher collision energies compared to low collision energies. Figure 19, shows the observed relative abundance of the superoxide-acetic acid adducts during measurements using the n = 4 cluster as the molecular ion at different collision energies. The pressure in the collision cell was held constant during these measurements.

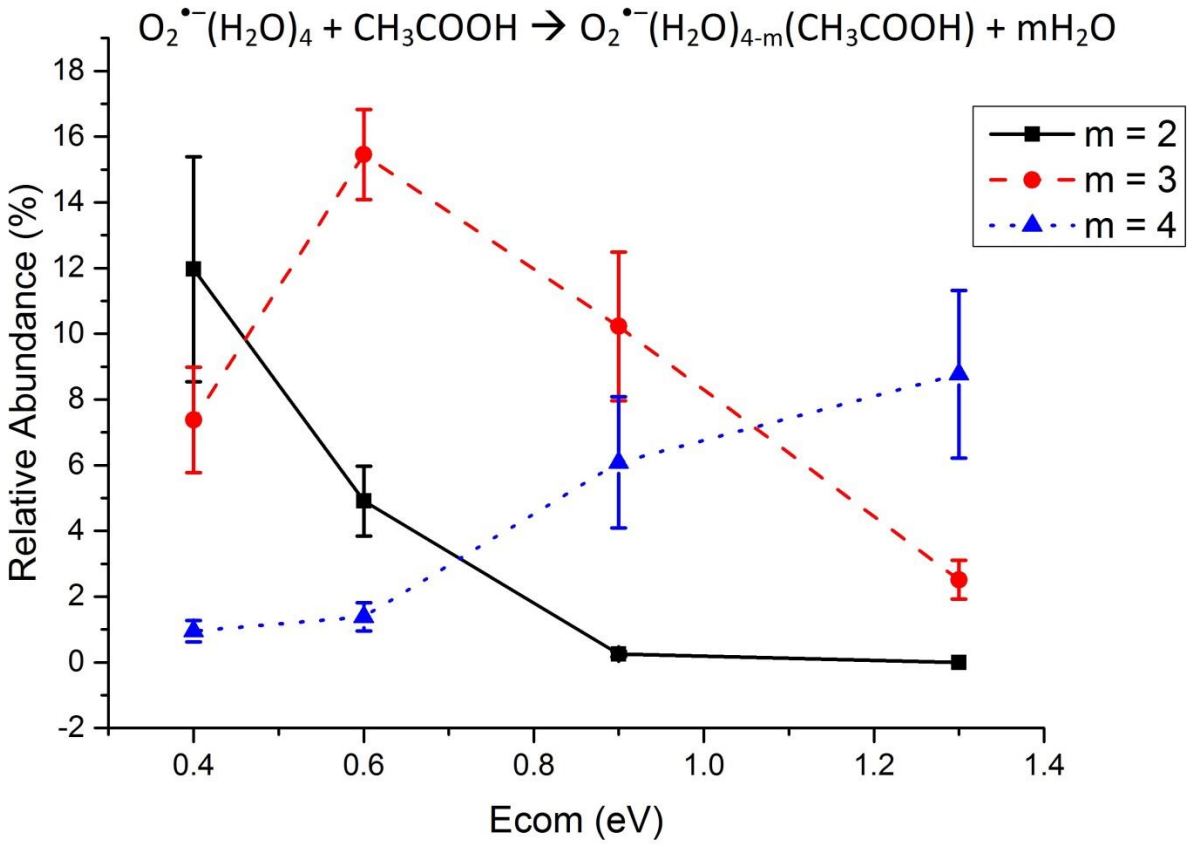

Figure 19: Plots for the relative abundance for the three $O_2^{\bullet-}(H_2O)_{4-m}(CH_3COOH)$ adducts plotted against the collision energy. The collision cell pressure was held constant at 1.80E-4 mBar.

Figure 19 shows an example of how the collision energy E_{com} affects the adducts formed through equation (38). At a low E_{com} of 0.4 eV, $O_2^{\bullet-}(H_2O)_2(CH_3COOH)$ has the highest relative abundance. As E_{com} was increased to 0.6 eV the relative abundance of this adduct decreased and the relative abundance $O_2^{\bullet-}(H_2O)(CH_3COOH)$ increased. When E_{com} was increased beyond 0.6 eV, the relative abundance of both the adducts decreased and an increase in the relative abundance of $O_2^{\bullet-}(CH_3COOH)$ was observed. This follows the reaction in equation (38), where m increases with the energy. It is worth noting that while the standard deviation increases with the relative abundance, the relative standard deviation stays approximately the same (~30%).

As for the deprotonation reaction, the relative abundance of the deprotonated product decreased when E_{com} was increased when using the n = 0 cluster. The opposite effect when the n = 1 cluster was used. This trend is displayed in Figure 20. The deprotonation reaction was not observed when using clusters larger than n = 1.

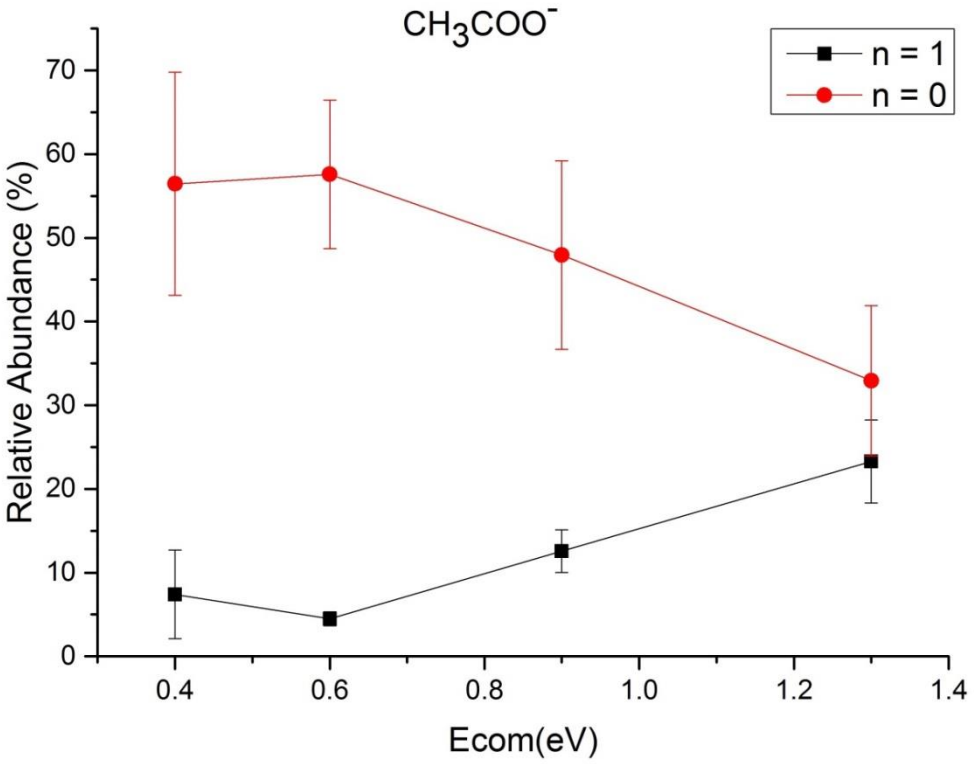

Figure 20: Plot of the relative abundance of the CH_3COO^- from the reaction $O_2^{\bullet-}(H_2O)_n + CH_3COOH \rightarrow CH_3COO^- + OOH^{\bullet} + nH_2O$ vs E_{com}. The collision cell pressure was held constant at 3.30E-4 mBar. The two plots are for n = 0 and n = 1.

3.3.3 - Pressure (P_{cell})

As the pressure in the collision cell is increased, the number of collision between the ions and the collision gas become more frequent. The abundance of the products increases with pressure and the observed abundance of unreacted water clusters decreases as collisions become more frequent with greater pressure.

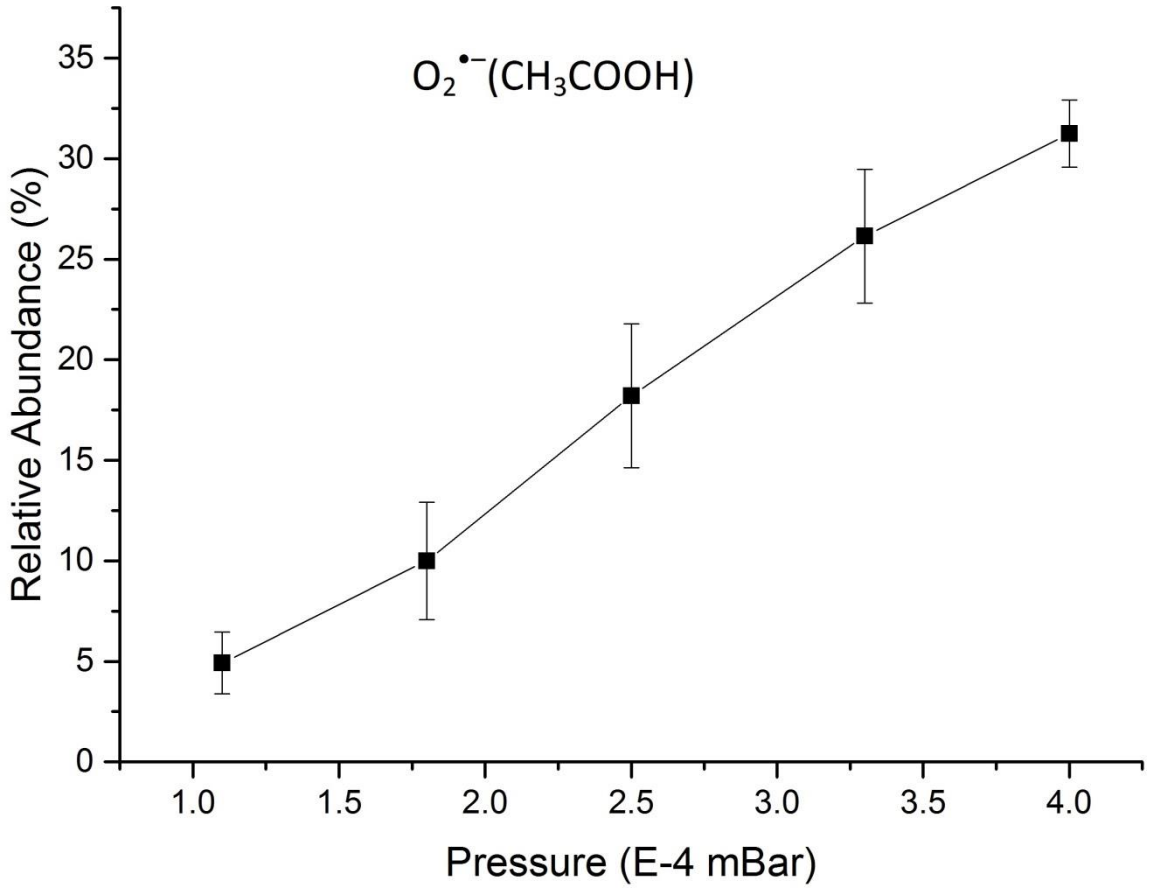

Figure 21: Plot of the relative abundance of $O_2^{\bullet-}(CH_3COOH)$ produced using the $O_2^{\bullet-}(H_2O)_2$ cluster and E_{com} = 1.3 eV at various pressures. The relative abundance seems to have a nearly linear dependence on the pressure, which is expected for this kind of reaction.

At increased pressures double collisions were observed in the form of $O_2^{\bullet-}(CH_3COOH)_2$ and $CH_3COO^-(CH_3COOH)$. While $CH_3COO^-(CH_3COOH)$ was observed no matter which cluster size was used, there was a significant increase in the relative abundance of this peak when the n = 1 cluster was used (Figure 22).

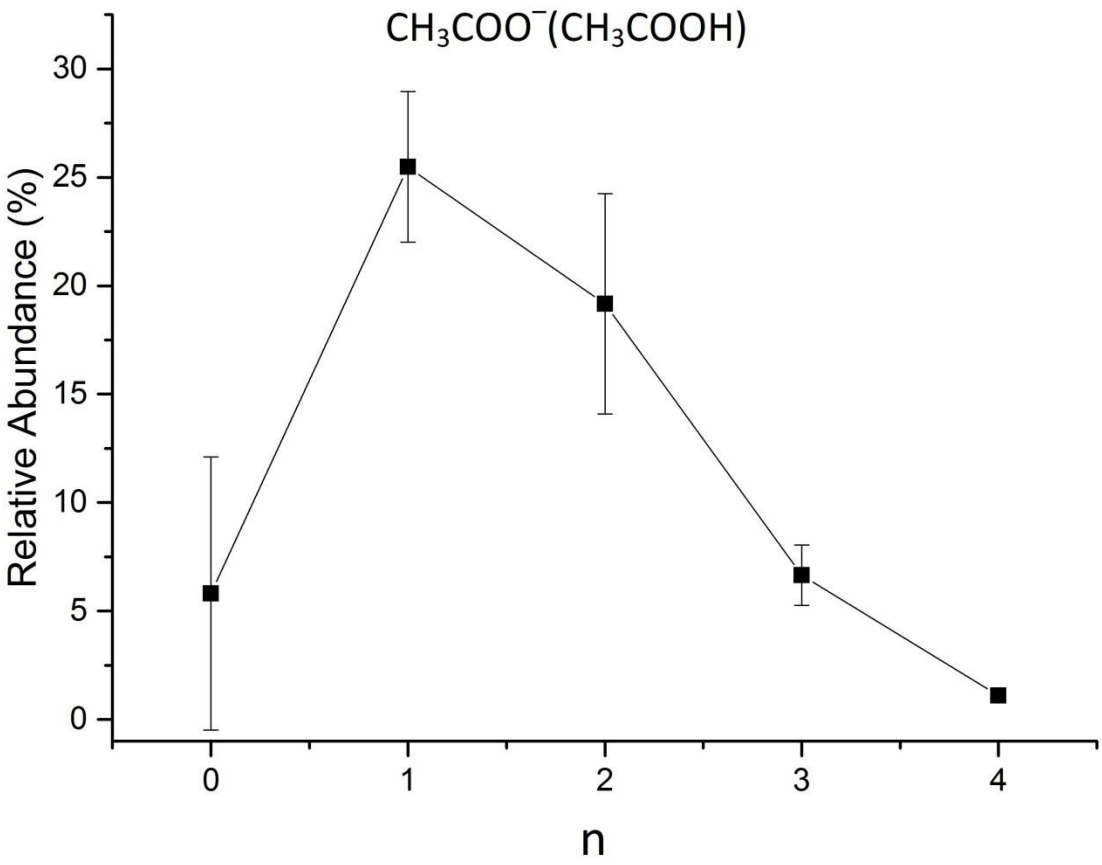

Figure 22: Plot of the relative abundance of $CH_3COO^-(CH_3COOH)$ as a function of cluster size, $O_2^{\bullet-}(H_2O)_n$ at a high pressure (4.00E-4 mBar) and a low E_{com} (0.4 eV). The production of this adduct is the greatest when n = 1. For n ≥ 2, a negative dependence on the cluster size is observed.

3.3.4 - Error sources

During a measurement, the signal intensity of the molecular ion is strongly dependent on the cluster size, E_{lab} (see equation (19) in section 2.4; an increase in E_{lab} will increase E_{com}) and the position of the electrospray needle. A low intensity of the molecular ion causes a lower total count of all products as fewer molecular ions are available for the reactions. This causes the sample size to go down and results in an increase in the uncertainty. This is particularly true for measurements where the $O_2^{\bullet-}$ anion was used and E_{lab} was low.

The positioning of the electrospray needle is a very subjective choice and may be difficult to reproduce. If the needle is positioned too close to the MS entrance, a discharge occurs which may damage the instrument, but the observed cluster production decreases exponentially with the distance

between the needle and the MS entrance. Because of this, placement of the needle requires careful positioning in order to maximize the signal while avoiding a discharge between the needle and the MS entrance. As an arbitrary requirement, the needle position was chosen so the blank measurement (n = 2, capillary voltage = 3.30 keV, cone voltage = 5-10 V, no collision gas) gave at least 300 counts/scan.

3.4 – Calculations

When considering the energy of the species from these calculations, only the sum of the electronic and zero-point energies have been used.

3.4.1 – Superoxide

Calculations on the superoxide anion revealed the n = 3, 4 clusters have more than one stable geometry conformations, but the planar conformation was found to be the most stable one which matches the stable quasi planar n = 3, 4 water clusters that have been observed before and discussed in earlier publications. [26, 43] The calculated structures of the water clusters n = 0 - 4 are shown in Figure 23.

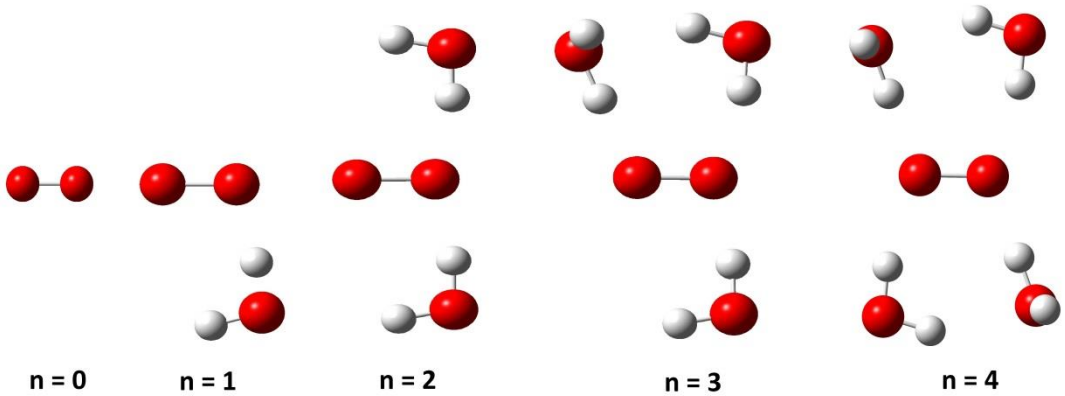

Figure 23: Calculated structure of the $O_2^{\bullet-}(H_2O)_n$ clusters, where n = 0 - 4. The geometries were determined through calculations using the B3LYP functional.

3.4.2 - Dimethyl disulphide

More than one stable conformation of the $O_2^{\bullet-}$(DMDS) adduct was predicted and this was indeed confirmed by quantum chemical calculations, however the conformation in which superoxide attacks sulfur in a nearly linear angle to the sulfur-sulfur bond was found to be the most stable conformation. This is a match with the observations made in a previous paper investigating nucleophilic substitution reactions on a similar disulphide system using quantum chemical calculation methods. [34]

An attempt was made to find a transition for the cleavage of the disulphide bond in the $O_2^{\bullet-}$(DMDS) complex. An energy profile was constructed by stretching the S-S bond and performing a transition state calculation using the geometry of the energy maxima found in the energy profile (Figure A - 4 and Figure A - 5 in the appendix). However, neither B3LYP, G4 nor MP2 were able to optimize such a transition state.

3.4.3 - Acetic acid

Geometry and energy optimizations was conducted on various species observed and as well as at different hydration levels. The energies of these species were then used to construct energy diagrams for the various products observed as well as possible intermediate products (Figure 26 through Figure 28).

4. Discussion

In this section, the experimental results will be compared to the results from the calculations which may paint a better picture of the system and the reactions that occur.

4.1 - Dimethyl disulphide

Experimental data indicates the reaction between a superoxide water cluster and DMDS to form an adduct was always accompanied by the loss of at least one water molecule; if no water molecules are present in the water cluster, the adduct will not be formed. Figure 24 shows the energy diagram for this reaction between $O_2^{\bullet-}(H_2O)$ and DMDS. The formation of 2DOH is strongly exothermic (-44 kJ/mol), and therefore very favourable; however this process generates a lot of heat and because the system is adiabatic, this energy has no way to leave the system, causing the adduct to become unstable. By evaporating the water molecule from the adduct, energy is removed from the system and 2DO is formed. Even if the overall reaction is slightly endothermic (9 kJ/mol), the ionization of the water cluster gives the reactants enough initial energy to form DO2. If the reactants have low initial energy, the loss of a single water molecule is enough to stabilize the system. If a larger water molecule had been used for this reaction, the adduct will have more water molecules available for this “energy removal” which would be necessary if the reactants have a higher initial energy. Similar energy diagrams for this reaction with water clusters of the size n = 2, 3, 4 are shown in the appendix, section 7.1, Figure A - 1 through Figure A - 3. The formation of these adducts are the most dominant in the recorded spectrums and their formation follows the reaction described in equation (37) at the end of section 3.2.4.

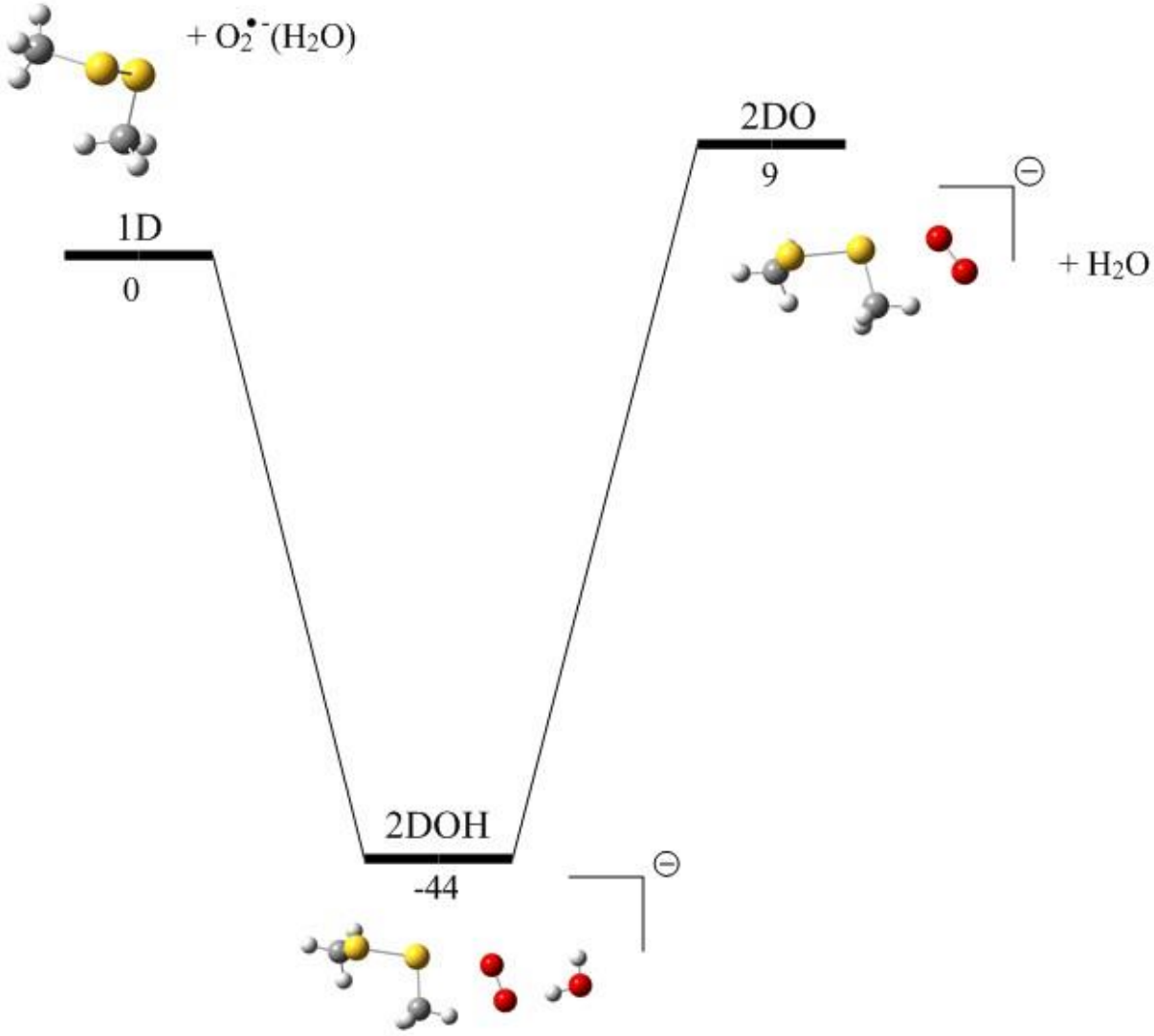

Figure 24: The energy diagram for the reaction between $O_2^{\bullet-}(H_2O)$ and DMDS. The energies are given in kJ/mol. These energies were calculated using the B3LYP functional with the aug-cc-pvtz basis set.

The spectrums where $O_2^{\bullet-}$ (n = 0) is the molecular ion are quite different from those where larger cluster sizes are the molecular ion and the energy diagram for this system is shown in Figure 25. The energy diagram shows the two species form the 2DO adduct and it is hypothesized this adduct may form two transition states; TS1 and TS2.

In TS1, the S-S bond is assumed to be stretched and the O-S bond is shortened. After overcoming the energy barrier of this transition state, the S-S bond is fully cleaved, forming either 1SO or 1SC through an endothermic reaction of 131 kJ/mol and 84 kJ/mol respectively. 1SO is thought to be capable of transitioning

into 1SO2, as this process is strongly exothermic (overall reaction enthalpy of -216), but calculations were unable to simulate a transition from the energy minima of 1SO to the energy minima of 1SO2. Thus no conclusion about the formation of this specie other than its formation enthalpy (-216 kJ/mol) can be made.

TS2 is assumed to be the result of migration of the superoxide anion to the methyl group, forming an O-C bond approximately coaxial to the S-C bond while weakening the S-C bond. This transition state is also assumed to be able to from 1D through a collision between $O_2^{\bullet -}$ at the carbon in the methyl group. From this transition state, the C-S bond can be fully cleaved, forming 2SC.

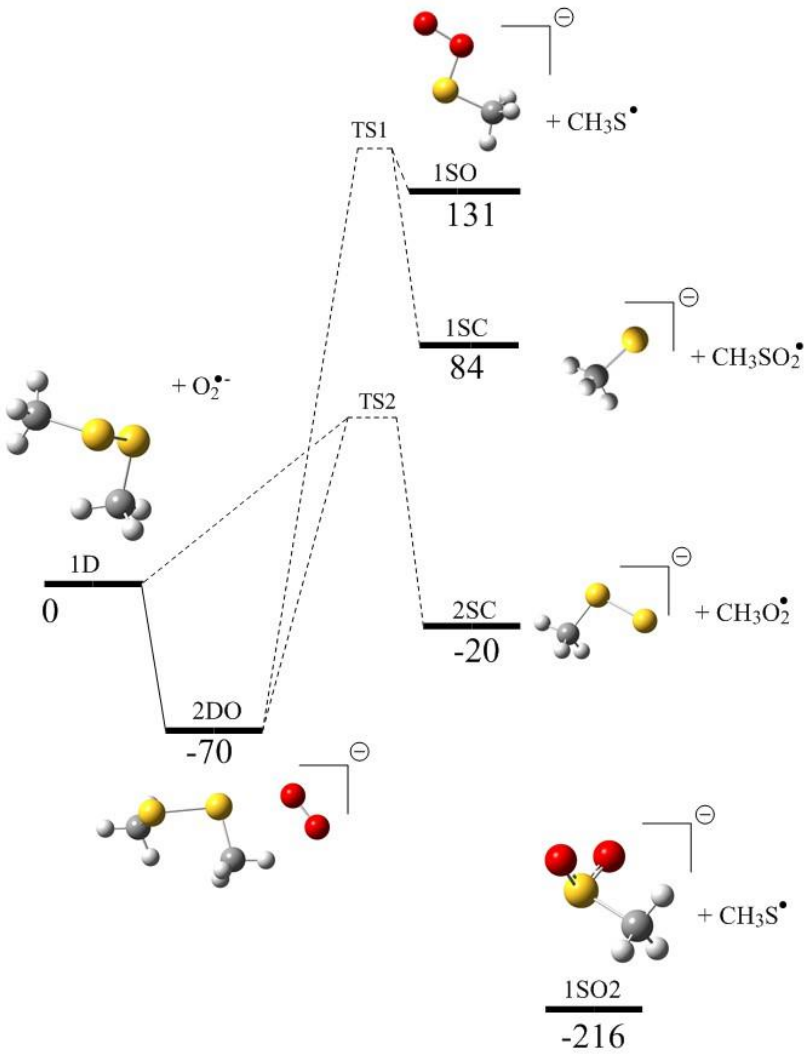

Figure 25: The energy diagram for the formation of $CH_3SO_2^-$ through the reaction between DMDS and $O_2^{\bullet -}$. The energies are listed in kJ/mol. These energies were calculated using the B3LYP functional with the aug-cc-pvtz basis set. Note: TS1 and TS2 could not be optimized with B3LYP; the heights of the energy barriers at these transition states are not representative for the real system. See text for further information.

Because no experimental observations of 1SO, 1SC or 2SC were made, the energy barriers of TS1 and TS2 are assumed to be significantly high. This explains why no reactions are observed when n = 0 water clusters were used; superoxide reacts with DMDS, forming 2DO. However, this exothermic process gives the products much excess energy which greatly destabilizes the sytem. Due to these high energy barriers of TS1 and TS2, the adduct cannot form any products and instead dissociates back to the reactants to reduce the amount of excess energy. When water clusters of $n \geq 1$ are used, the adduct is formed and water molecules are vaporized to remove the excess energy. The adduct don't have enough energy to overcome the energy barriers, nor does it have enough energy to dissociate back into the reactants, thus the adduct is observed in the mass spectrum.

Calculations were unable to determine energy or structure of neither TS1 nor TS2. This could be due to poor initial geometry for the transition state calculations. The initial geometry was chosen based on the energy profile from the stretching of the S-S bond (the energy profile is shown in Figure A - 4 in the appendix). The energy profile has a discontinuity however, due to what appears to be the formation of a weak S-H bond between the sulphur on the leaving group and the hydrogen atoms on the methyl group (Figure A - 5). This discontinuity in the energy profile could lead to an energy maximum that is not the result of the dissociation of the S-S bond, resulting in a poor initial geometry for the transition state calculations. A second reason why the calculations failed at finding these transition states could be that the methods used (B3LYP, G4 and MP2) are poorly suited for transition state calculations for these systems.

4.2 - Acetic acid

The formation of the observed adducts follows the expected trends for these kinds of systems. The fact that the adduct $O_2^{\bullet-}(CH_3COOH)$ is only observed when a water molecule is vaporized indicates that the adduct formation is exothermic. This is confirmed by quantum chemical calculations in Figure 26; the adduct formation (1CO) is a strongly exothermic process and in an adiabatic system, this excess energy cannot be removed through the collisions with

nearby molecules. The adduct becomes unstable due to all the excess energy stored inside it and releases it through dissociation into CH_3COO^- (2C). The overall reaction enthalpy for this reaction is slightly exothermic (-20 kJ/mol according to calculations).

When water clusters of n ≥ 1 are used, the water molecules provide a way for the system to release energy through evaporation of the water molecules, allowing for stabilization of the intermediate adducts, thus these adducts are observed in spectrums where these water clusters are the molecular ion. The energy diagrams for this reaction using larger water clusters can be found in the appendix, section 7.2.1.

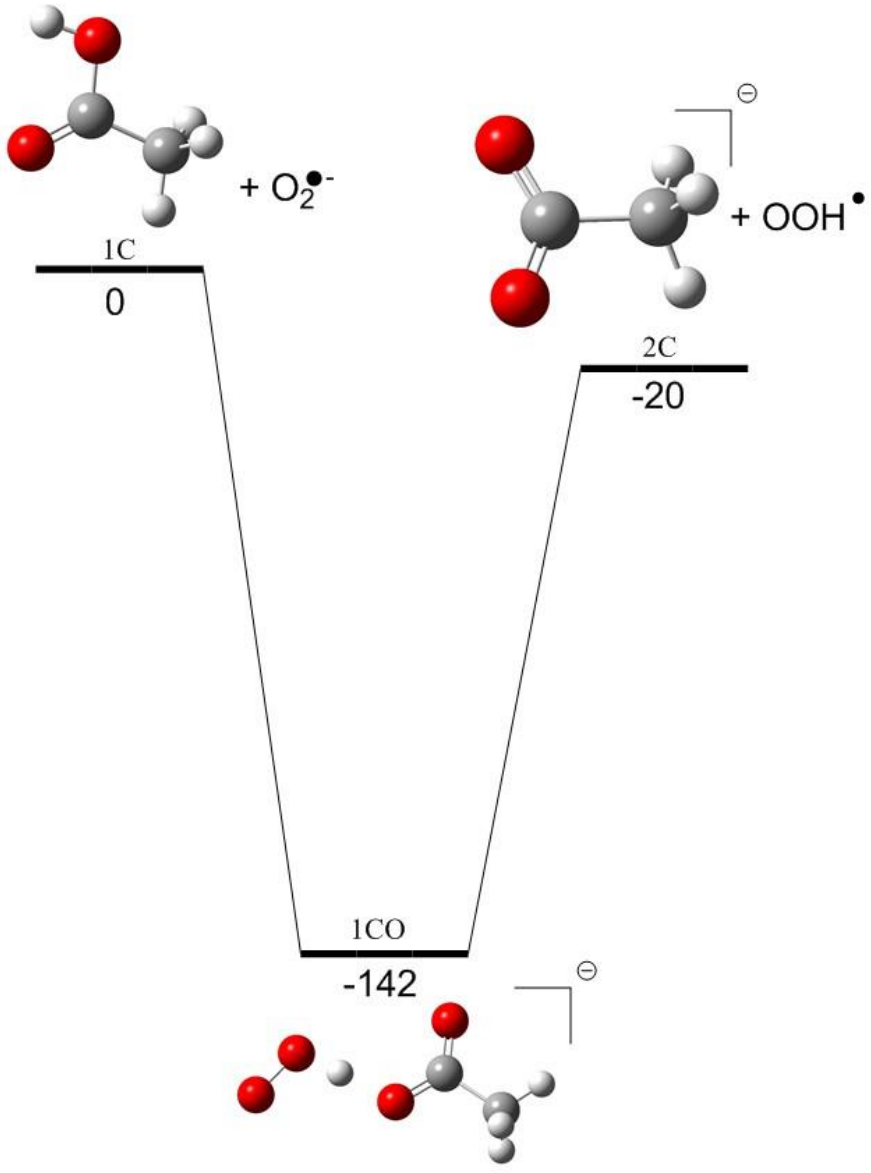

Figure 26: Energy diagram displaying the reaction pathway for the reaction described in equation (39). The energies are listed in kJ/mol and were calculated using the B3LYP functional with the aug-cc-pvtz basis set.

Table 6 shows the gas phase basicity of fluorine, superoxide, acetate and chlorine, whose values are in good agreement with the claim that the gas phase basicity of superoxide is be between that of chlorine and fluorine, but above acetate. [16, 27, 44]. The gas phase basicity for superoxide was calculated using experimental values found in the literature. These calculations are shown in the appendix, section 7.2.2.

Table 6: The gas phase basicity of the species fluorine, superoxide, acetate and chlorine. The gas phase basicity of superoxide is based on calculations using the electron affinity of oxygen, ionization potential of hydrogen and the H-O bond energy in H-$O_2^{\bullet}$. The remaining gas phase basicity of the other species are collected from the NIST library.

Specie	Gas phase basicity (kJ/mol)
F^-	1530
$O_2^{\bullet-}$	1466
CH_3COO^-	1427
Cl^-	1373

This shows the superoxide anion has higher gas phase basicity than acetate, allowing superoxide to deprotonate acetic acid. Because the gas phase basicity is defined as the Gibbs free energy for the deprotonation reaction, the Gibbs free energy for the reaction will be the difference in gas phase basicity between superoxide and acetate, which is -39 kJ/mol. This can be compared to the estimated Gibbs free energy for the reaction in Figure 26 which was calculated to be -20 kJ/mol. Some discrepancy in these values are expected, as the values in the energy diagram are zero point vibrational energy, so the temperature is set to 0K while experimental values are for standard conditions. It appears the values provided by B3LYP are of the same magnitude as the experimental values. The conclusion is the values provided by B3LYP are fine to use for a qualitative analysis.

The observation of $CH_3COO^-(CH_3COOH)$ when the n = 1 water cluster is used is interesting and raises the question as to what its reaction pathway is. One possible pathway for the formation is displayed in Figure 27, named reaction pathway A. The 1CO1H adduct is formed in an exothermic process, giving the products more excess energy. This pathway is very similar to the one outlined in Figure 26. Instead of evaporation of the water molecule, a hydrogen dioxide radical is formed and released from the complex, forming 2C1H which has less excess energy. A second collision with another acetic acid molecule then

occurs, causing the formation of the 3CH complex, which is unstable due to the high excess energy from the exothermic process. The removal of the water molecule reduces this excess energy, producing the observed 3C product. In this pathway, the 2C1H complex seems to have much less excess energy, giving it a long enough lifetime to allow the second collision to occur. The 2C1H complex is observed in experiments with low pressure and low collision energies; however their abundance is much lower than expected, indicating this pathway may not be very favourable and a different pathway is also possible.

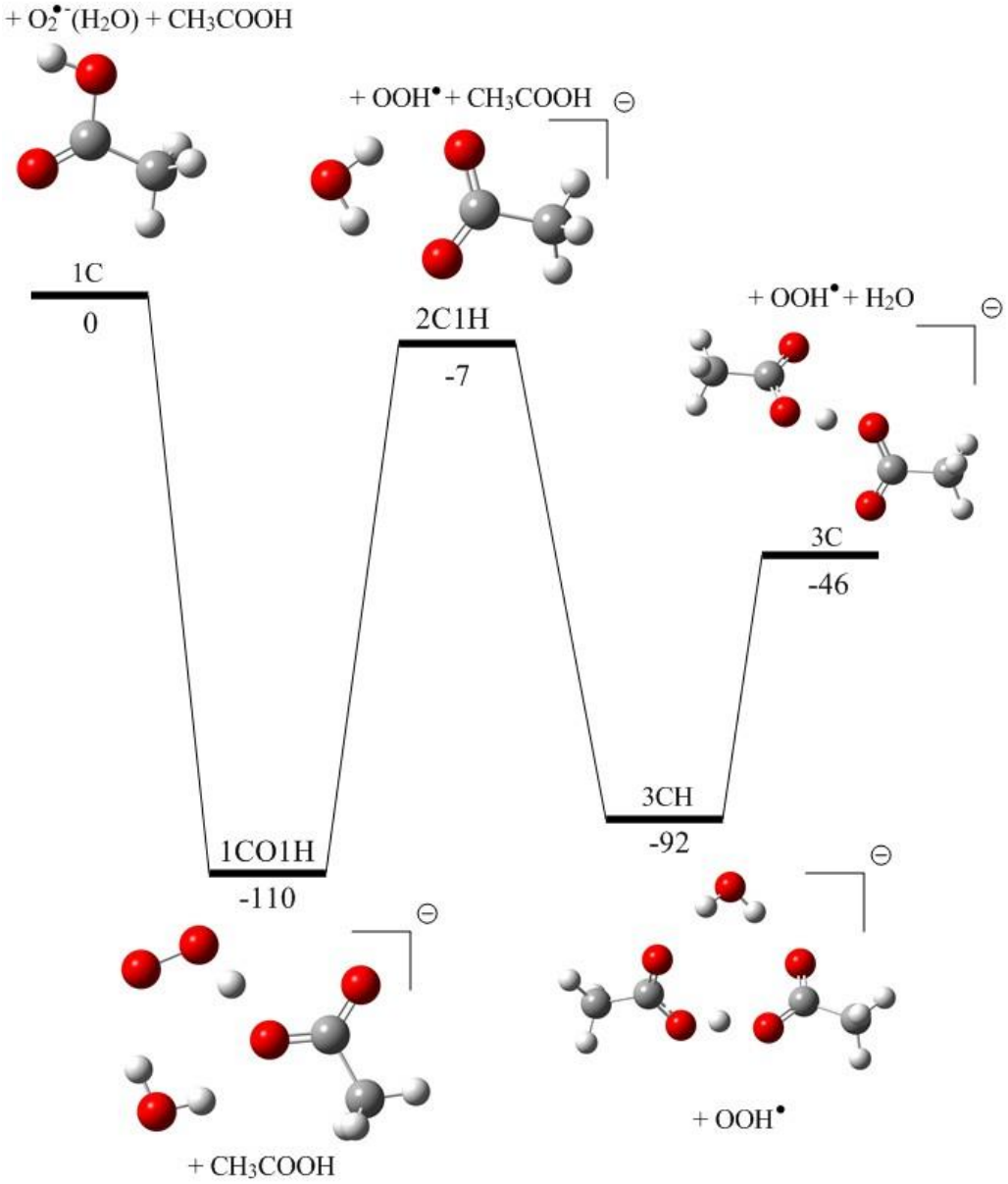

Figure 27: Reaction pathway A for the production of $CH_3COO^-(CH_3COOH)$ with the n = 1 cluster. The energies are listed in kJ/mol and were calculated using the B3LYP functional with the aug-cc-pvtz basis set.

Reaction pathway B (Figure 28) is a similar pathway, but involves the production of the 1CO adduct, which then undergoes a second collision with acetic acid, forming the 3CO species. This specie has much excess energy and due to this is highly unstable, readily dissociating into 3C. This reaction pathway seems to be more favourable compared to pathway A, as much more of 1CO (pathway B) is observed compared to 2C1H (pathway A) despite 1CO seemingly having more excess energy.

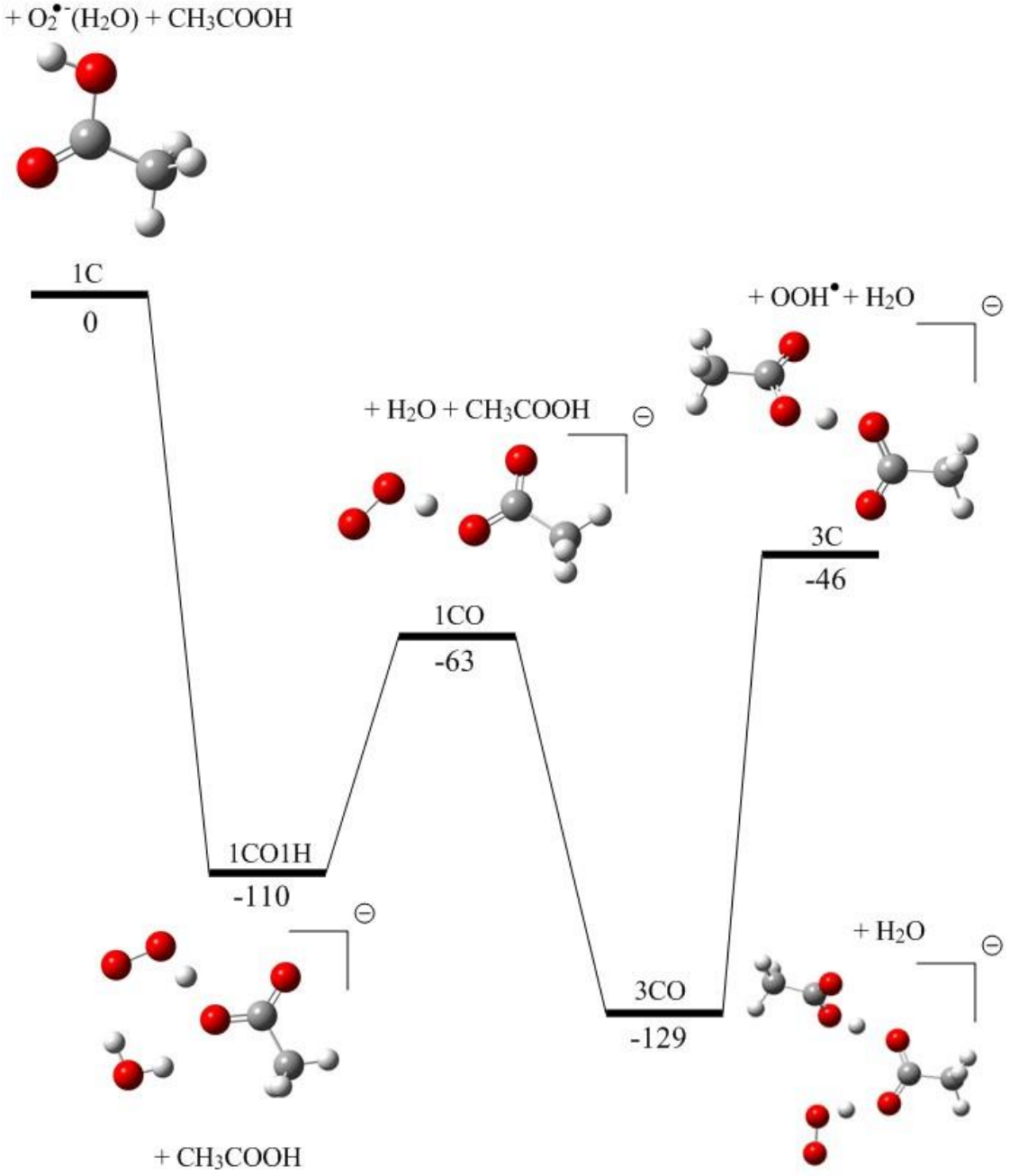

Figure 28: Reaction pathway B for the production of $CH_3COO^-(CH_3COOH)$ with the n = 1 cluster. The energies are listed in kJ/mol and were calculated using the B3LYP functional with the aug-cc-pvtz basis set.

5. Conclusion

5.1 - Dimethyl disulphide

Very few reactions were observed between the water clusters and DMDS. Adduct formations between DMDS and the water clusters were the vast majority of the products observed. While small amounts of what seems to be CH_3S^- is observed, the signal of this peak was very low and no conclusion can be made about it. If CH_3S^- is formed, the reason for the low abundance of this signal could be explained by the energy diagram in

Figure 25; the formation of this species has a presumably very high energy barrier, hindering the reaction. This is confirmed by the fact that small amounts of this specie are only observed at higher energies when n = 1 - 4 is used. More investigation into this reaction under different conditions would be preferred.

5.2 - Acetic acid

Acetic acid and the superoxide water clusters of n = 1 – 4 readily forms adducts. When higher energies are used, one or more water molecules may be lost, depending on the excess energy of the product. When the n = 0 anion is the molecular ion, only deprotonated acetic acid is formed, no adduct formation is observed. This deprotonation is due to superoxide having a higher proton affinity than acetate.

The production of $CH_3COO\_(CH_3COOH)$ from the n = 1 water cluster have two possible pathways. While both pathways are possible, pathway B seems to be the most favourable one. This is probably due to the loss of $OOH^\bullet$ while leaving the H_2O attached to the complex is not an easy reaction; the straight up loss of a water molecule in pathway B seems much more favourable.

Extrapolating these results to bulk solution seems to indicate direct deprotonation will not happened in bulk solution as the presence of water greatly stabilizes the adduct form. However, this may give the adduct a long enough lifetime to possibly gain enough energy for the deprotonation at a later time.

6. References

1. Kandola, K., A. Bowman, and M.A. Birch-Machin, *Oxidative stress – a key emerging impact factor in health, ageing, lifestyle and aesthetics.* International Journal of Cosmetic Science, 2015. **37**: p. 1-8.
2. Schieber, M. and N. Chandel, *ROS Function in Redox Signaling and Oxidative Stress.* Current Biology. **24**(10): p. R453-R462.
3. Dröge, W., *Free Radicals in the Physiological Control of Cell Function.* Physiological Reviews, 2002. **82**(1): p. 47-95.
4. Jin, Y.N., W.Y. Hwang, C. Jo, and G.V.W. Johnson, *Metabolic State Determines Sensitivity to Cellular Stress in Huntington Disease: Normalization by Activation of PPAR?* PLoS ONE, 2012. **7**(1): p. e30406.
5. Bhat, A.H., K.B. Dar, S. Anees, M.A. Zargar, A. Masood, M.A. Sofi, and S.A. Ganie, *Oxidative stress, mitochondrial dysfunction and neurodegenerative diseases; a mechanistic insight.* Biomedicine & Pharmacotherapy, 2015. **74**: p. 101-110.
6. Koyama, T., M. Tawa, N. Yamagishi, A. Tsubota, T. Sawano, M. Ohkita, and Y. Matsumura, *Role of superoxide production in post-ischemic cardiac dysfunction and norepinephrine overflow in rat hearts.* Eur. J. Pharmacol., 2013. **711**(1–3): p. 36-41.
7. Elchuri, S., T.D. Oberley, W. Qi, R.S. Eisenstein, L. Jackson Roberts, H. Van Remmen, C.J. Epstein, and T.-T. Huang, *CuZnSOD deficiency leads to persistent and widespread oxidative damage and hepatocarcinogenesis later in life.* Oncogene, 2004. **24**(3): p. 367-380.
8. Zelko, I.N., T.J. Mariani, and R.J. Folz, *Superoxide dismutase multigene family: a comparison of the CuZn-SOD (SOD1), Mn-SOD (SOD2), and EC-SOD (SOD3) gene structures, evolution, and expression.* Free Radical Biol. Med., 2002. **33**(3): p. 337-349.
9. Imlay, J.A., *The molecular mechanisms and physiological consequences of oxidative stress: lessons from a model bacterium.* Nat Rev Micro, 2013. **11**(7): p. 443-454.
10. Austin, S., E. Klimcakova, and J. St-Pierre, *Impact of PGC-1α on the topology and rate of superoxide production by the mitochondrial electron transport chain.* Free Radical Biol. Med., 2011. **51**(12): p. 2243-2248.
11. Halliwell, B. and J.M.C. Gutteridge, *[1] Role of free radicals and catalytic metal ions in human disease: An overview*, in *Methods Enzymol.* 1990, Academic Press. p. 1-85.
12. Halliwell, B., M.V. Clement, and L.H. Long, *Hydrogen peroxide in the human body.* FEBS Lett., 2000. **486**(1): p. 10-13.
13. Khurshid, S.S., J.A. Siegel, and K.A. Kinney, *Technical Note: Particulate reactive oxygen species concentrations and their association with environmental conditions in an urban, subtropical climate.* Atmos. Chem. Phys., 2014. **14**(13): p. 6777-6784.
14. Anglada, J.M., M. Martins-Costa, J.S. Francisco, and M.F. Ruiz-López, *Interconnection of Reactive Oxygen Species Chemistry across the Interfaces of Atmospheric, Environmental, and Biological Processes.* Acc. Chem. Res., 2015. **48**(3): p. 575-583.
15. Halliwell, B., *Role of Free Radicals in the Neurodegenerative Diseases.* Drugs & Aging, 2012. **18**(9): p. 685-716.
16. Hayyan, M., M.A. Hashim, and I.M. AlNashef, *Superoxide Ion: Generation and Chemical Implications.* Chem. Rev., 2016. **116**(5): p. 3029-3085.
17. Blanksby, S.J., V.M. Bierbaum, G.B. Ellison, and S. Kato, *Superoxide Does React with Peroxides: Direct Observation of the Haber–Weiss Reaction in the Gas Phase.* Angew. Chem. Int. Ed., 2007. **46**(26): p. 4948-4950.
18. Ryding, M.J., A. Debnárová, I. Fernández, and E. Uggerud, *Nucleophilic Substitution in Reactions between Partially Hydrated Superoxide Anions and Alkyl Halides.* J. Org. Chem., 2015. **80**(12): p. 6133-6142.
19. Merritt, M.V. and D.T. Sawyer, *Electrochemical studies of the reactivity of superoxide ion with several alkyl halides in dimethyl sulfoxide.* J. Org. Chem., 1970. **35**(7): p. 2157-2159.

20. Johnson, R.A., E.G. Nidy, and M.V. Merritt, *Superoxide chemistry. Reactions of superoxide with alkyl halides and alkyl sulfonate esters.* JACS, 1978. **100**(25): p. 7960-7966.
21. Yu, D., D.A. Armstrong, and A. Rauk, *The transition probability of electron loss from anions in the gas phase: The lifetime of O2 ·−.* J. Chem. Phys., 1992. **97**(8): p. 5522-5531.
22. Peterson, D.A., S.L. Archer, and E.K. Weir, *Superoxide Reduction of a Disulfide: A Model of Intracellular Redox Modulation?* Biochem. Biophys. Res. Commun., 1994. **200**(3): p. 1586-1591.
23. Hirsikko, A., T. Nieminen, S. Gagné, K. Lehtipalo, H.E. Manninen, M. Ehn, U. Hõrrak, V.M. Kerminen, L. Laakso, P.H. McMurry, A. Mirme, S. Mirme, T. Petäjä, H. Tammet, V. Vakkari, M. Vana, and M. Kulmala, *Atmospheric ions and nucleation: a review of observations.* Atmos. Chem. Phys., 2011. **11**(2): p. 767-798.
24. Tanner, S.D., G.I. Mackay, and D.K. Bohme, *An experimental study of the reactivity of the hydroxide anion in the gas phase at room temperature, and its perturbation by hydration.* Can. J. Chem., 1981. **59**(11): p. 1615-1621.
25. Beyer, M.K., *Hydrated metal ions in the gas phase.* Mass Spectrom. Rev., 2007. **26**(4): p. 517-541.
26. Niedner-Schatteburg, G. and V.E. Bondybey, *FT-ICR Studies of Solvation Effects in Ionic Water Cluster Reactions.* Chem. Rev., 2000. **100**(11): p. 4059-4086.
27. Dzidic, I., D.I. Carroll, R.N. Stillwell, and E.C. Horning, *Gas phase reactions. Ionization by proton transfer to superoxide anions.* JACS, 1974. **96**(16): p. 5258-5259.
28. Alon, T. and A. Amirav, *How enhanced molecular ions in Cold EI improve compound identification by the NIST library.* Rapid Commun. Mass Spectrom., 2015. **29**(23): p. 2287-2292.
29. Ho, C.S., C.W.K. Lam, M.H.M. Chan, R.C.K. Cheung, L.K. Law, L.C.W. Lit, K.F. Ng, M.W.M. Suen, and H.L. Tai, *Electrospray Ionisation Mass Spectrometry: Principles and Clinical Applications.* Clinical Biochemist Reviews, 2003. **24**(1): p. 3-12.
30. Mason, E. *Diagram of Electrospray Ionization.* 2015 21 January 2015; Available from: https://commons.wikimedia.org/wiki/File:Electrospray_Ionization_Spectroscopy.svg.
31. Iavarone, A.T. and E.R. Williams, *Mechanism of Charging and Supercharging Molecules in Electrospray Ionization.* JACS, 2003. **125**(8): p. 2319-2327.
32. Gross, J.H., *Mass Spectrometry: A Textbook*. 2011. p. 117-210.
33. Paul, W., *Electromagnetic traps for charged and neutral particles.* Reviews of Modern Physics, 1990. **62**(3): p. 531-540.
34. Bachrach, S.M. and D.C. Mulhearn, *Nucleophilic Substitution at Sulfur: SN2 or Addition−Elimination?* J. Phys. Chem., 1996. **100**(9): p. 3535-3540.
35. Gross, J.H., *Mass Spectrometry: A Textbook*. 2011. p. 420-423.
36. Elisemarion, *Français : analyseur de spectrométrie de masse à temps de vol (time of flight TOF) schématisé, avec le trajet des ions, en mode réflectron*. 2007.
37. Atkins, P. and R. Friedman, *Molecular Quantum Mechanics*. 5th edition ed. 2011.
38. Szabo, A. and N.S. Ostlund, *Modern Quantum Chemistry: Introduction to Advanced Electronic Structure Theory*. First Edition, Revised ed. 1996.
39. Cramer, C.J., *Essentials of Computational Chemistry: Theories and Models*. 2004. p. 249-300.
40. Bach, R.D., O. Dmitrenko, and C. Thorpe, *Mechanism of Thiolate−Disulfide Interchange Reactions in Biochemistry.* J. Org. Chem., 2008. **73**(1): p. 12-21.
41. Arshadi, M. and P. Kebarle, *Hydration of OH- and O2- in the gas phase. Comparative solvation of OH- by water and the hydrogen halides. Effects of acidity.* J. Phys. Chem., 1970. **74**(7): p. 1483-1485.
42. Kang, J.K. and C.B. Musgrave, *Prediction of transition state barriers and enthalpies of reaction by a new hybrid density-functional approximation.* J. Chem. Phys., 2001. **115**(24): p. 11040-11051.

43. Ludwig, R., *Water: From Clusters to the Bulk.* Angew. Chem. Int. Ed., 2001. **40**(10): p. 1808-1827.
44. Shen, V.K., D.W. Siderius, W.P. Krekelberg, and H.W. Hatch, eds. *NIST Standard Reference Simulation Website*. NIST Standard Reference Database Number 173. National Institute of Standards and Technology, Gaithersburg MD, 20899, http://doi.org/10.18434/T4M88Q, retrieved 9th of May 2017.

7. Appendix

7.1 – DMDS

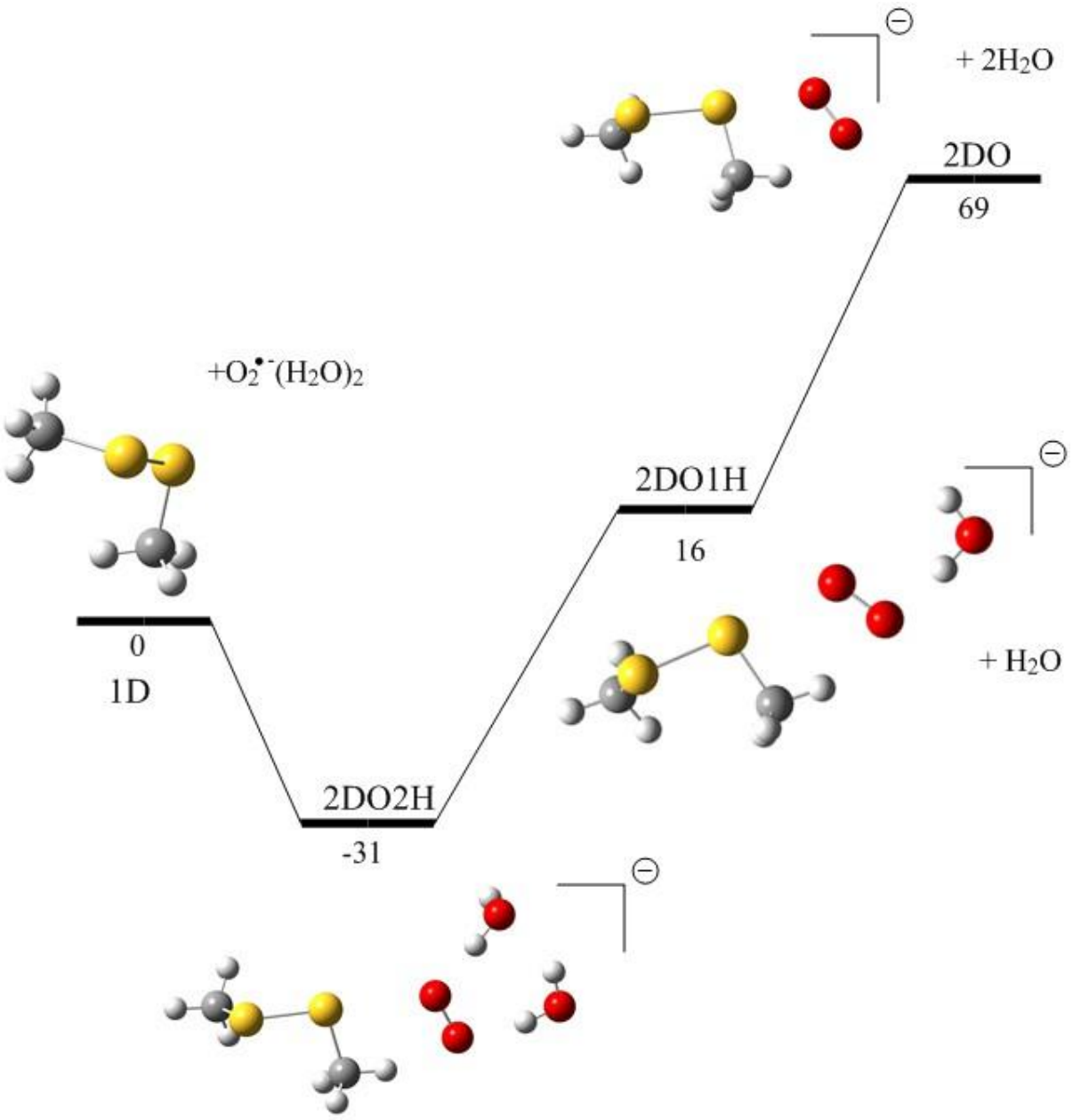

Figure A - 1: The energy diagram for the reaction between $O_2^{\bullet-}(H_2O)_2$ and DMDS. The energies are given in kJ/mol were calculated using the B3LYP functional with the aug-cc-pvtz basis set.

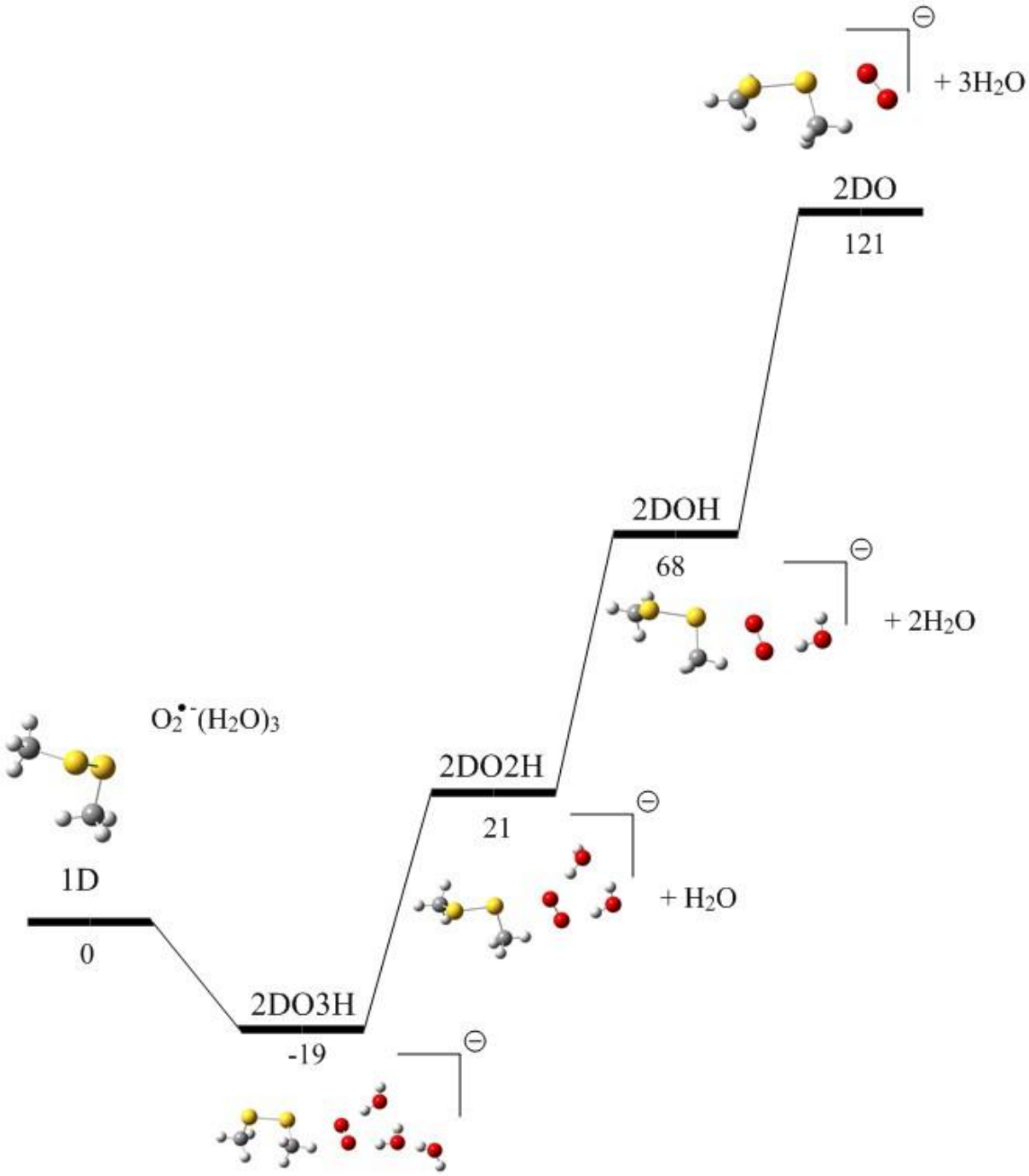

Figure A - 2: The energy diagram for the reaction between $O_2^{\bullet-}(H_2O)_3$ and DMDS. The energies are given in kJ/mol were calculated using the B3LYP functional with the aug-cc-pvtz basis set.

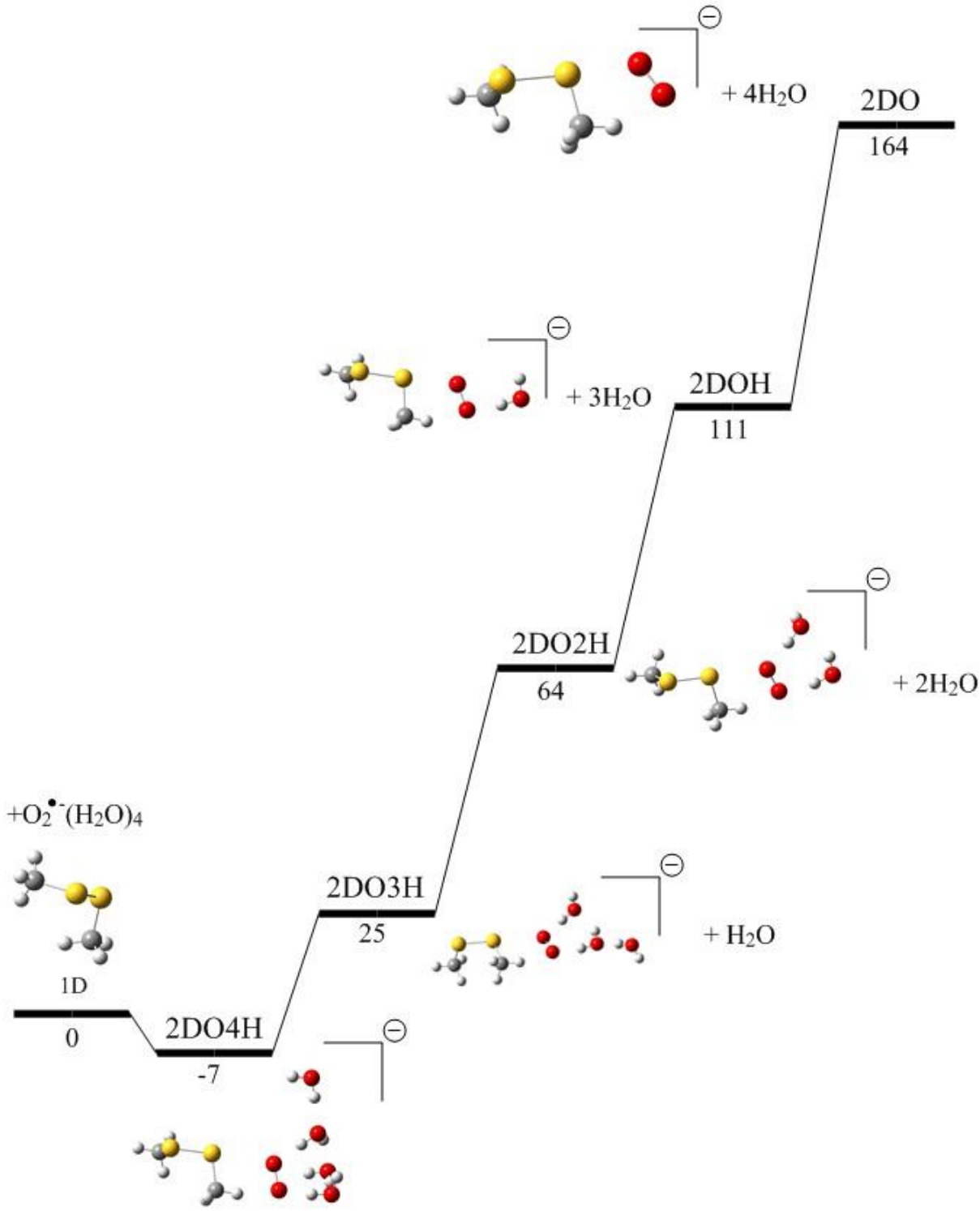

Figure A - 3: The energy diagram for the reaction between $O_2^{\bullet-}(H_2O)_4$ and DMDS. The energies are given in kJ/mol were calculated using the B3LYP functional with the aug-cc-pvtz basis set.

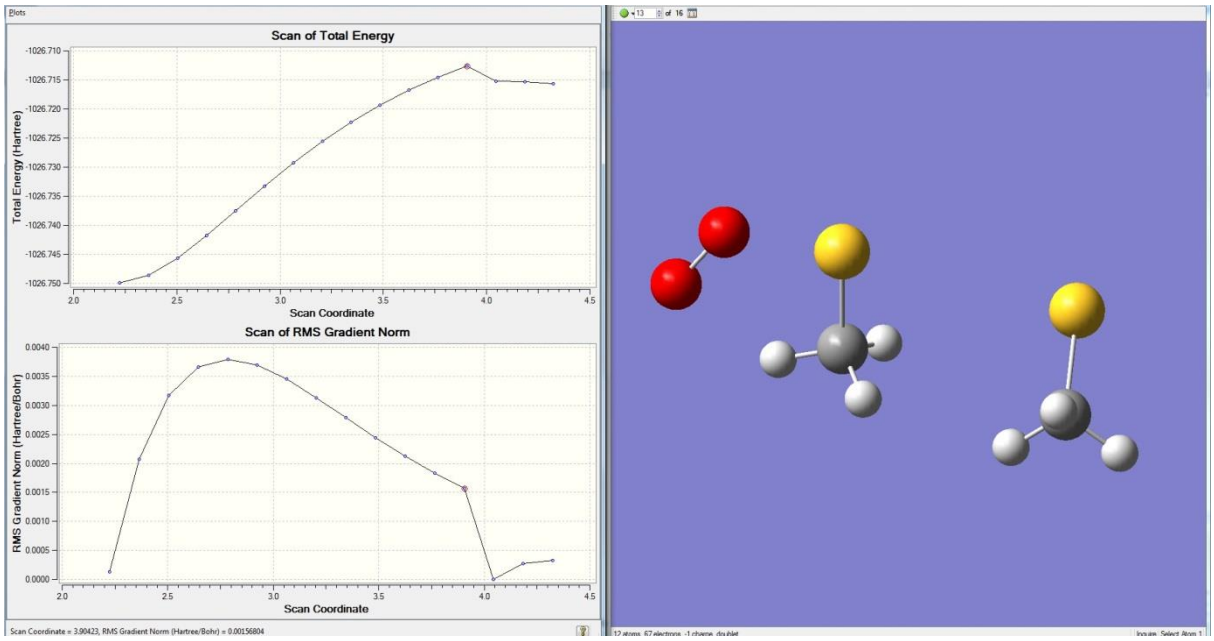

Figure A - 4: The energy profile from the stretching of the S-S bond is shown on the left and the geometry of the complex at the energy maxima is shown on the right. As seen on the energy profile, the energy of the complex increases as the S-S bond is stretched, until a discontinuity appears in the energy profile, at which point the energy starts decreasing as the bond is stretched further.

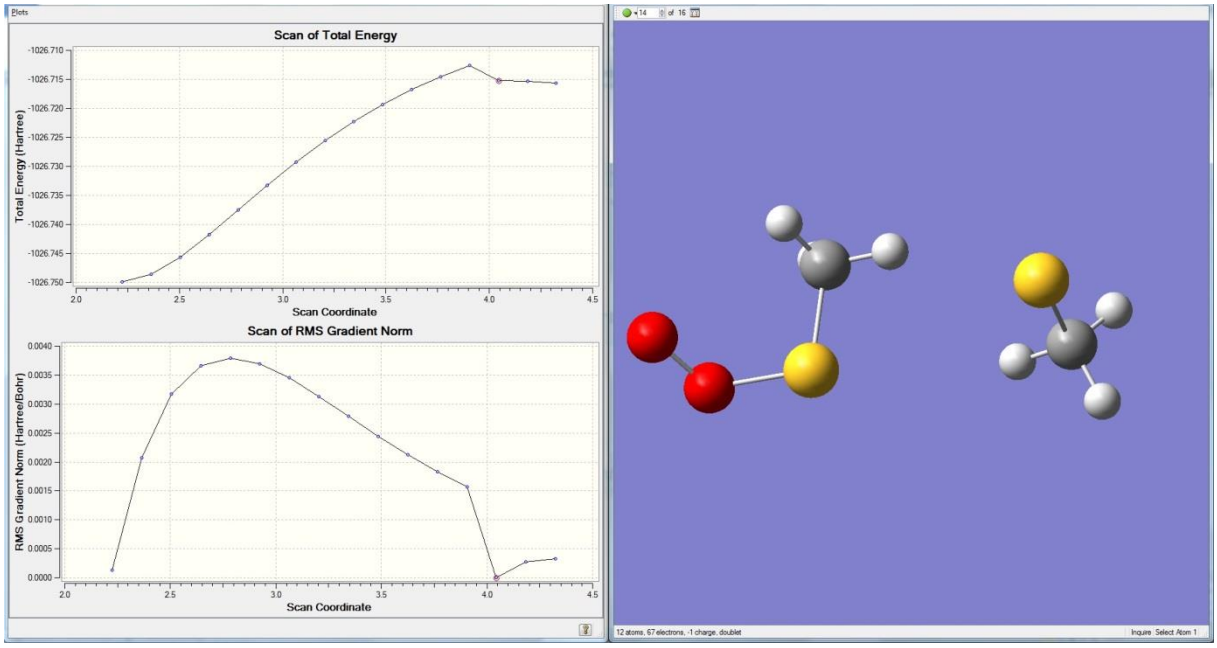

Figure A - 5: The energy profile from the stretching of the S-S bond is shown on the right. The picture on the right shows the geometry of the $O_2^{\bullet-}$(DMDS) complex at the point which the discontinuity in the energy profile appears. Here, the $CH_3S^{\bullet}$ group has rotated, to bring the sulphur atom closer to the hydrogen atom on the nearby CH_3-group, indicating a weak bond has formed between them.

7.2 – Acetic Acid

7.2.1 – Energy diagrams for acetic acid

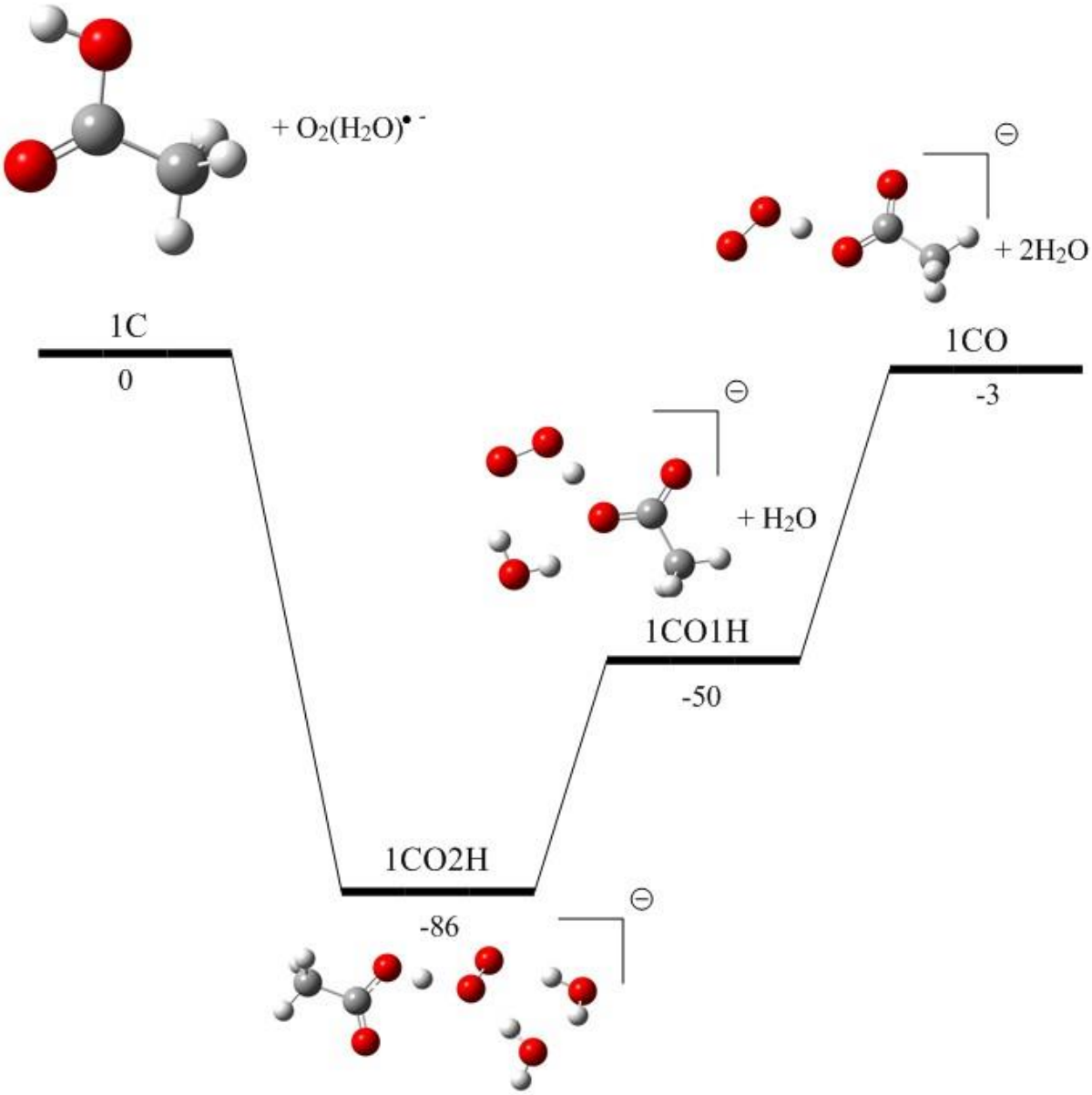

Figure A - 6: Energy diagram for the formation and stepwise dehydration of $O_2^{\bullet-}(H_2O)_2(CH_3COOH)$ from the reaction between $O_2^{\bullet-}(H_2O)_2$ and acetic acid. The energies are given in kJ/mol were calculated using the B3LYP functional with the aug-cc-pvtz basis set.

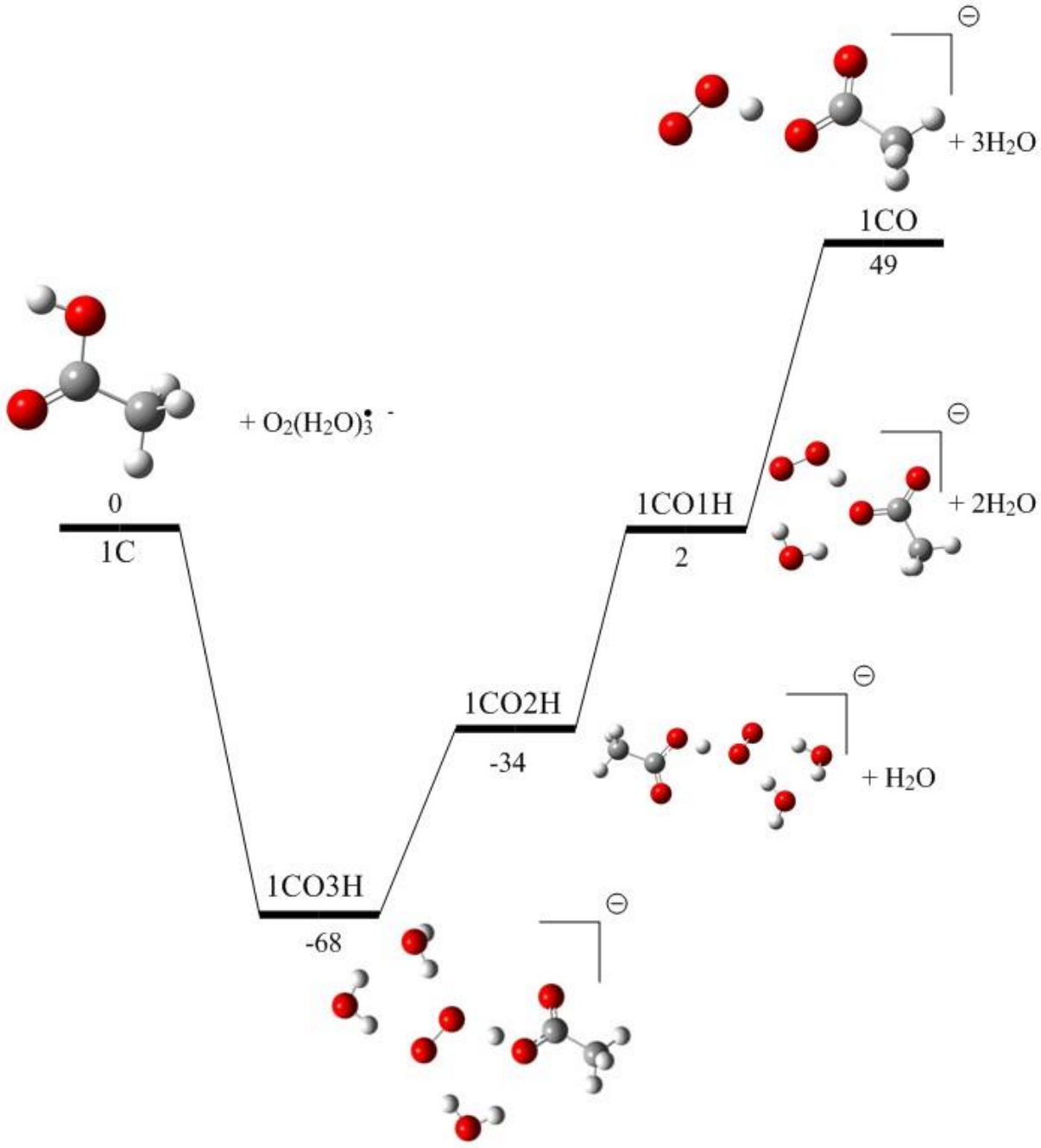

Figure A - 7: Energy diagram for the formation and stepwise dehydration of $O_2^{\bullet-}(H_2O)_3(CH_3COOH)$ from the reaction between $O_2^{\bullet-}(H_2O)_3$ and acetic acid. The energies are given in kJ/mol were calculated using the B3LYP functional with the aug-cc-pvtz basis set.

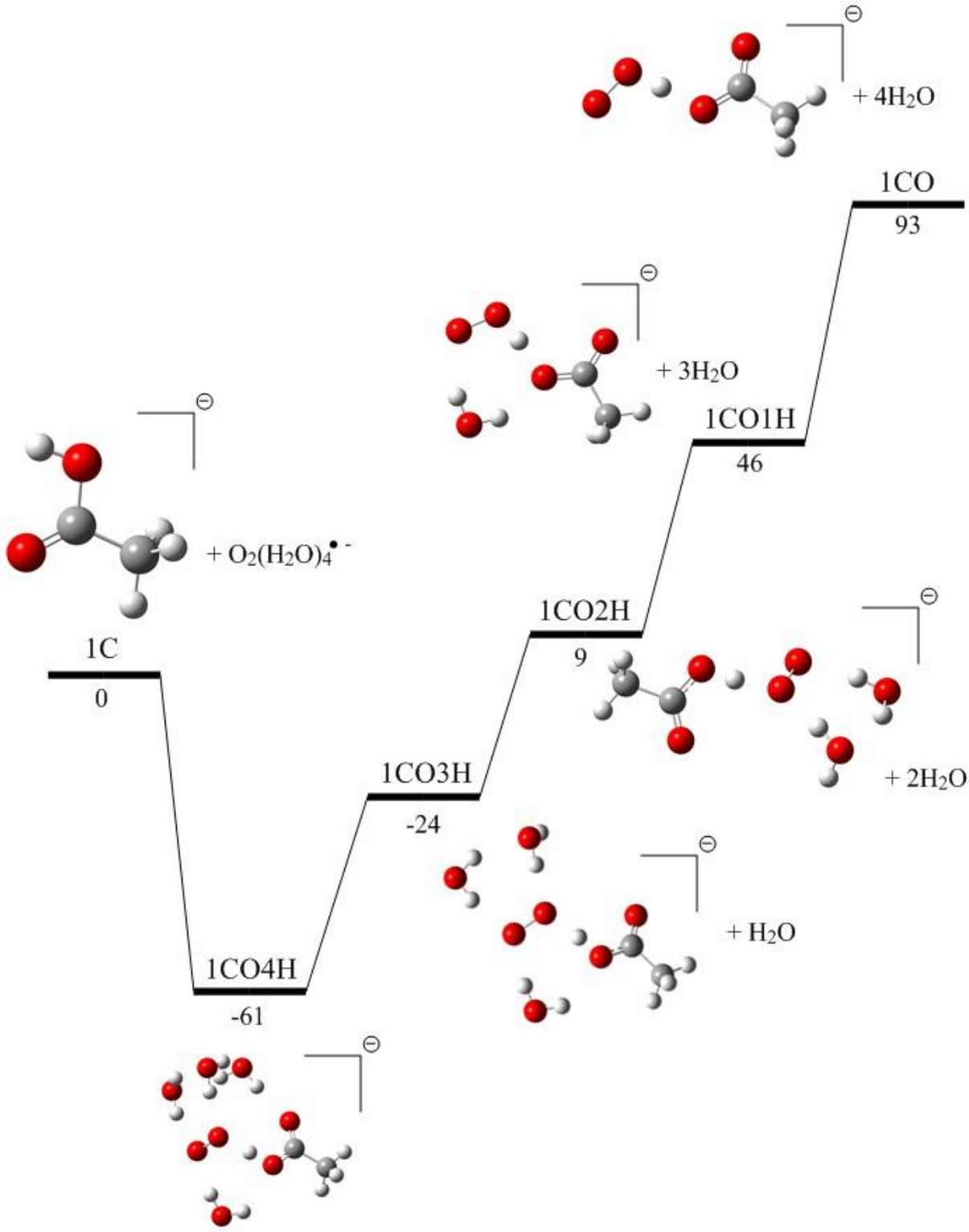

Figure A - 8: Energy diagram for the formation and stepwise dehydration of $O_2^{\bullet-}(H_2O)_4(CH_3COOH)$ from the reaction between $O_2^{\bullet-}(H_2O)_4$ and acetic acid. The energies are given in kJ/mol were calculated using the B3LYP functional with the aug-cc-pvtz basis set.

7.2.2 – Calculation of the gas phase basicity of $O_2^{\bullet-}$

This reaction is explained by considering the gas phase basicity of the species involved in the reaction. The proton affinity of superoxide can be calculated through the stepwise reactions that occur during the overall reaction. The overall reaction is

$$HO_2 \rightarrow H^+ + O_2^{\bullet-} \tag{40}$$

The energy of the overall reaction can be described by the energies of the stepwise reactions: the ionization potential (IP) of oxygen, the electron affinity (EA) of hydrogen and the bond energy of the O-H bond (D(H-$O_2^{\bullet-}$)).

$$EA(O_2) \qquad O_2 + e^- \rightarrow O_2^{\bullet-} \tag{41}$$

$$IP(H) \qquad H^+ + e^- \rightarrow H \tag{42}$$

$$D(H - O_2^{\bullet}) \qquad H^+ + O_2^{\bullet-} \rightarrow H - O_2^{\bullet} \tag{43}$$

$$GB(O_2^{\bullet-}) = D(H - O_2^{\bullet}) + IE(H) - EA(O_2) \tag{44}$$

The values of EA(O_2) has been determined to be 43 kJ/mol, IP(H) has been determined to be 1312 kJ/mol eV and D(H-$O_2^{\bullet}$) to be 197 kJ/mol. On the basis of these values, using equation (44) gives superoxide a gas phase basicity of 1466 kJ/mol. These values are taken from the following references. [27, 44]